

Frisch Konstantin (Orcid ID: 0000-0002-9198-6754)

Voigt Silke (Orcid ID: 0000-0002-2560-5933)

Verestek Verena (Orcid ID: 0000-0001-5847-4354)

Albert Roper Richard (Orcid ID: 0000-0002-0185-8581)

Raddatz Jacek (Orcid ID: 0000-0002-5713-9682)

Weber Yuki (Orcid ID: 0000-0002-3037-6338)

Batenburg Sietske, J. (Orcid ID: 0000-0002-4076-1248)

Long-period astronomical forcing of westerlies' strength in Central Asia during Miocene climate cooling

KONSTANTIN FRISCH¹, SILKE VOIGT¹, VERENA VERESTEK², ERWIN APPEL², RICHARD ALBERT¹, AXEL GERDES¹, IRIS ARNDT¹, JACEK RADDATZ¹, THOMAS VOIGT³, YUKI WEBER⁴, and SIETSKJE J. BATENBURG⁵

¹Institut für Geowissenschaften, Goethe-Universität, Altenhöferallee 1, 60438-Frankfurt am Main, Germany (E-mail: frisch@em.uni-frankfurt.de)

²Fachbereich Geowissenschaften, Eberhard-Karls-Universität, Hölderlinstr. 12, 72074-Tübingen, Germany

³Institut für Geowissenschaften, Friedrich-Schiller-Universität, Burgweg 11, 07749-Jena, Germany

⁴Department of Earth and Planetary Sciences, Harvard University, 20 Oxford Street, Cambridge MA 02138, USA

⁵Géosciences Rennes, Université de Rennes 1, Campus de Beaulieu, 35042 Rennes, France

Corresponding author: Konstantin Frisch (frisch@em.uni-frankfurt.de)

This article has been accepted for publication and undergone full peer review but has not been through the copyediting, typesetting, pagination and proofreading process which may lead to differences between this version and the Version of Record. Please cite this article as doi: 10.1002/palo.20802

Abstract

The continental expression of global cooling during the Miocene Climate Transition (MCT) in Central Asia is poorly documented, as the tectonically active setting complicates the correlation of Neogene regional and global climatic developments. This study presents new geochemical data (CaSO_4 content, carbonate $\delta^{13}\text{C}$ and $\delta^{18}\text{O}$) from the endorheic alluvial-lacustrine Aktau succession (Ili Basin, south-east Kazakhstan) combined with findings from the previously published facies evolution. Time series analysis revealed long eccentricity forcing of the paleohydrology throughout the entire succession, split into several facies-dependent segments. Orbital tuning, constrained by new laser ablation U-Pb dates and a pre-existing magnetostratigraphy, places the succession in a 5.0 Ma long interval in the Middle to Late Miocene (15.6 to 10.6 Ma). The long-term water accumulation in the Ili Basin followed the timing of the MCT, suggesting increased precipitation in the catchment area in response to climate cooling and stronger westerly winds. This was paced by minima of the 2.4 Ma eccentricity cycle, that favoured the establishment of a discharge playa (~14.3 Ma) and a perennial lake (12.6 to 11.8 Ma). Furthermore, low obliquity amplitudes (nodes) caused a transient weakening of the westerlies at ~13.7 to 13.5 Ma and at ~12.7 Ma, resulting in negative hydrological budgets and salinization. Flooding of the windward Ili Basin coeval with aridification in the leeward basins suggests that the Tian Shan was a climate boundary already in the Middle Miocene. Our results emphasize the impact of climate fluctuations on the westerlies' strength and thus on Central Asian hydrology.

Plain Language Summary

The global climate changed from an exceptional warm to a colder state in the Middle Miocene Epoch, representing a milestone in the evolution of today's climate. This study focuses on the, so far fragmentary, understanding of the Central Asian climate response to this global climate transition by investigating deposits of a former (salt) lake in the Ili Basin, south-east Kazakhstan. Regular sediment alternations represent

cycles of low and high water level, overprinted by a long-term lake expansion. Time series analysis of climate sensitive geochemical and environmental parameters, together with the determination of absolute rock ages, enabled the identification of sedimentary cycles (405 ka and 1.2 Ma long), which are equivalent to climate influencing variations of the Earth's orbit and tilt angle. We conclude that water level maxima are linked to periods of low seasonal climate differences re-occurring every 405 ka. The lake expansion is caused by more precipitation due to strengthened westerly winds, in response to global cooling. Westerly winds were transiently weakened during periods of low variability of the Earth's tilt angle, promoting high evaporation and salinization. Our results emphasize the impact of climate change on the westerlies' strength and thus on Central Asian moisture supply.

Key Points:

- 1 The endorheic Miocene Ili Basin features orbital control of its hydrological budget by long eccentricity and obliquity amplitude modulation.
- 2 Obliquity amplitude modulation affected the westerlies's strength during the Miocene Climate Transition.
- 3 The Miocene global cooling led to strengthening of the westerlies reflected by groundwater accumulation and lake expansion in the Ili Basin.

Keywords: Orbital forcing, Continental climate, Central Asia, Miocene cooling, Integrated stratigraphy

1. INTRODUCTION

The global Miocene climate evolution is characterised by a period of pronounced cooling during the Miocene Climate Transition (MCT), which terminated the exceptional warmth of the Miocene Climatic Optimum (MCO) and marked the beginning of a sustained climate deterioration, culminating in the modern ice-house mode (e.g. Zachos et al., 2001). The MCT is well documented in marine sediments by a series of positive shifts in the $\delta^{18}\text{O}$ of benthic foraminifera (Mi3a, Mi3b and Mi4), which correspond to glaciation events on Antarctica (Miller et al., 1991, 1996; Flower & Kennett, 1994; Westerhold et al., 2005; Holbourn et al., 2013). This Middle Miocene cooling has also been recognized in numerous continental climate archives from the Northern Hemisphere and likely contributed to the step-wise process of the Neogene mid-latitude aridification in North America and Eurasia (Flower & Kennett, 1994; Eronen et al., 2012; Miao et al., 2012; Pound et al., 2012; Frisch et al., 2019). Additionally, the extent and marine connectivity of the Paratethys as a potential source for moisture uptake is crucial for Eurasian climate during the Cenozoic (Ramstein et al., 1997; Karami et al., 2011; Bosboom et al., 2014; Bougeois et al., 2018; Meijer et al., 2019). Despite a general aridification trend, there is evidence for sustained humid conditions in Central Asia (Akhmetiev et al., 2005) and western Eurasia through the Middle Miocene with increasing amounts of annual precipitation in the early Late Miocene (van Dam, 2006; Bruch et al., 2011; Böhme et al., 2011; Eronen et al., 2012). In Central Asia, the correlation of regional climate turnovers with the global Neogene climate evolution is complicated by tectonically induced diachroneities and heterogeneous subsidence history of basins associated with the building of the Tian Shan mountain complex (Macaulay et al., 2014 and references therein). This led to a differentiation into locally diverging precipitation trends (Miao et al., 2012; Caves Rugenstein & Chamberlain, 2018).

This study presents the effects of orbital forcing and global cooling on the hydrological evolution of the alluvial-lacustrine Ili Basin in south-east Kazakhstan, during a period

of steady basin subsidence in the Middle to Late Miocene. In lacustrine settings, particularly in hydrologically closed basins like the Miocene Ili Basin, insolation changes exert a control on the water budget, often resulting in an orbital control on sedimentation (van Vugt et al., 1998; Abels et al., 2009, 2010; Smith et al., 2014). An integrated age model, based on a detailed cyclostratigraphic framework combined with magnetostratigraphy and age constraints from laser ablation U-Pb dating, is proposed for the Aktau succession. This integrated approach allows a profound assessment of the hydrological evolution, i.e. the balance of evaporation and precipitation, by disentangling the effects of orbital forcing and global climate change on the regional climate in the Ili Basin. The reconstruction of wind systems requires a strict differentiation of a mostly arid to semi-arid basin centre from a more humid catchment area, analogous to the modern climate state. Our results demonstrate the control of long-period eccentricity cycles on basin hydrology and the impact of the 1.2 Ma cycle of obliquity amplitude modulation on the intensity of the westerlies. The Middle to Late Miocene lake expansion in the Ili Basin during and after the MCT is discussed in the context of global cooling, which likely favoured strengthening of the westerly winds with increased rainout in the windward areas of the Tian Shan.

2. GEOGRAPHICAL, GEOLOGICAL AND CLIMATOLOGICAL SETTING

The Ili Basin is situated within the Tian Shan mountain complex in the territories of south-east Kazakhstan and the Xinjiang Province, China (Fig. 1a, Frisch et al. (2019) provided a detailed geographic overview). The intracontinental Tian Shan orogen was formed as far-field response to the India-Asia collision and first showed substantial uplift rates around the Oligocene-Miocene transition (Hendrix et al., 1994; Sobel et al., 2006; Macaulay et al., 2014), which became accelerated in the Middle to Late Miocene (Bullen et al., 2003; Charreau et al., 2005, 2009; Sun & Zhang, 2009; Macaulay et al., 2014; Zhang, T. et al., 2014, De Pelsmaeker et al., 2015). In response to the Tian Shan's orogeny and progressive crustal deformation, the Ili Basin formed as a foreland basin

(Kober et al., 2013), and experienced alternating periods of endorheic and exorheic conditions. Sedimentation started in the Late Eocene and comprises alluvial-lacustrine and fluvial deposits in the basin centre (Lucas et al., 2000), whereas the margins are dominated by alluvial fan conglomerates intercalated with frequent paleosols (Hellwig et al., 2018). Increased crustal compression during and after the Pleistocene exposed the Cenozoic basin fill in a series of W-E striking anticlines (Kober et al., 2013), one of them hosting the Aktau ('White Mountains') succession (44.03°N and 79.30°E, Figs. 1b and c).

The Aktau succession consists of more than 1000 m of basinal Cenozoic sediments (Fig. 2), which are continuously exposed along the northern limb of the south-verging anticline. An overview of the Cenozoic (bio)stratigraphy of the Aktau succession is given in Nigmatova et al. (2018) and summarized in Figure 2. From ~320 to 740 m, Middle to Upper Miocene formations (abbreviated Fm) comprise reddish-brownish mudstones with thin-sheeted sandstones and gypcretes (Bastau Fm), multi-colored marls, mudstones and gypcretes (Koktal Fm) and greyish marls and limestones with reddish-brownish gypsiferous mudstones (Kokterek Fm) (Bazhanov & Kostenko, 1961; Bodina 1961; Voigt et al., 2017). Parent rocks are Permo-Carboniferous volcanics of the Central Asian Orogenic Belt (Ili-Balkhash volcanic arc; Jahn et al., 2004; Kröner et al., 2014) that are exposed today in subordinate mountain ranges 10 to 30 km north of the Aktau. The studied succession (stretching from ~320 to 700 m in the entire Aktau succession) is framed by fluvial sandstones and conglomerates of the Upper Oligocene-Lower Miocene Aidarly Formation and fossiliferous fluvial to lacustrine mud- and siltstones of the Upper Miocene-Pliocene Ili Formation (Bazhanov & Kostenko, 1961; Dzhamangaraeva, 1997; Lucas et al., 1997; Kordikova, 2000; Kordikova & de Bruijn, 2001). A recently published magnetostratigraphy by Verestek et al. (2018) places the Bastau Fm in the Langhian.

At present, the climate of the Ili Basin is characterised by a bimodal distribution of monthly precipitation with the main peak in spring and early summer and a less

pronounced increase of rainfall in autumn (Sun, H. et al., 2010). This pattern results from the annual migration of the westerly jet, which interacts with the Tian Shan, leading to considerable orographic rainfall in the mountain ranges (Schiemann et al., 2009). There, the average annual precipitation exceeds the value of 250 to 500 mm a⁻¹ reported for the lowland plains of the Ili Basin (Sun, H. et al., 2010).

3. MATERIAL AND METHODS

Logging, sampling strategy and outcrop positions of the Aktau succession were described in Voigt et al. (2017) and Frisch et al. (2019). Time series analysis was performed on records of (i) element geochemistry (CaSO₄, sampling interval 0.5 m), (ii) stable isotopes of carbonates ($\delta^{13}\text{C}$, sampling interval 0.5 m) and (iii) a semi-quantitative facies-derived record of water levels (Frisch et al., 2019) with a spacing of 0.25 m. Paleoclimatic interpretations are supported by the records of $\delta^{18}\text{O}$ and facies-derived salinity (Frisch et al., 2019).

3.1 Element geochemistry

The element geochemistry record is a composite of published data (0-83 m; Voigt et al. (2017) and new measurements for this study (83-322 m). The sulphur content of bulk-sediments was determined at the Goethe-University Frankfurt by microwave digestion and ICP-OES analysis. 100 mg of sample powder was digested in HF-enhanced aqua regia (2 mL HNO₃, 5 mL HCl, 1 mL HF) in an Anton Paar Multiwave 3000 microwave oven. The solution was diluted (1:14) and analysed on an iCAP6300 Duo by Thermo Scientific with Yttrium as internal standard to account for plasma matrix effects. The reproducibility of the analyses was determined by repeated digestion and measurement of an internal whole-procedure reference material (N=7), resulting in an uncertainty of 10% (2 σ). The sulphur concentration of samples was used for the stoichiometric calculation of the bulk rock CaSO₄ content. The acetic acid

leachable and residue fractions published in Voigt et al. (2017) were summed to enable comparison to the whole-rock element contents presented here.

3.2 Stable isotope ($\delta^{13}\text{C}$ and $\delta^{18}\text{O}$) measurements

Oxygen and carbon isotopes were analysed on bulk-rock samples at the Institute of Geosciences, Goethe-University Frankfurt. The rock powder was digested in 96% phosphoric acid at 72°C and analysed as CO_2 using a Finnigan MAT 253 mass spectrometer (Thermo Scientific) coupled to a Thermo Gas Bench II in continuous flow mode. Values are reported relative to the Vienna Pee Dee Belemnite (VPDB) standard through the analysis of an in-house standard calibrated to NBS-19. The analytical uncertainty of $\delta^{13}\text{C}$ and $\delta^{18}\text{O}$ analyses repeated standard measurements is better than 0.04‰ and 0.07‰, respectively. Further, the signal intensities at mass 44 are used to estimate the carbonate content in order to detect potential dependencies of the related stable isotope signal.

3.3 Laser ablation U-Pb dating

Laser ablation U-Pb dating of carbonates is a geochronological method which has been successfully used to acquire radiometric ages from paleosols (Methner et al. 2016; Hellwig et al., 2018; Liivamägi et al., 2018) and to date diagenetic carbonate precipitates (Li et al., 2014; Godeau et al., 2018; Mangenot et al., 2018). The approach used here is a modification of the method Gerdes & Zeh (2006, 2009), described in detail in Methner et al. (2016). Here, we apply this method on primary carbonates from lacustrine and mudflat environments.

Samples were screened and analysed in situ from polished sections using a RESOLution S-155 (Resonetics) 193 nm ArF Excimer laser (CompexPro 102, Coherent) equipped with a two-volume ablation cell (Laurin Technic) coupled to a sector field ICP-MS (Element 2, Thermo) at the Goethe-University, Frankfurt following the method of Gerdes and Zeh (2006, 2009).

Ablation was performed in a He atmosphere (0.3 l/min) and mixed in the ablation funnel with 1.03 l min⁻¹ Ar and 0.07 l min⁻¹ N. Static ablation used a spot size of 213 µm and a fluence of c. 1.5 J cm⁻² at 12 Hz. Each analysis consists of 19 s background acquisition followed by 18 s of sample ablation and 20 s washout. During data acquisition, the signals of ²⁰⁶Pb, ²⁰⁷Pb, ²³²Th and ²³⁸U were detected by peak jumping in pulse counting mode with a total integration time of 0.1 s. SRM-NIST 614 (N=26) was used as primary reference to correct for mass bias (²⁰⁷Pb/²⁰⁶Pb, c. 0.3%) and inter-element fractionation (²⁰⁶Pb/²³⁸U, c. 3%) and their drift through the entire analytical sequence (c. 12 h). After correcting for drift, mass bias, inter-element fractionation and 7% matrix-offset, the WC-1 (N=26) common Pb-corrected ²⁰⁶Pb/²³⁸U ratio reproduced over the three consecutive days to 252.7±1.0 Ma (2σ, MSWD=1.02, Mean Square Weighted Deviation, MSWD=1.02). A stromatolitic limestone from the Cambrian-Precambrian boundary in South-Namibia (Feldschuhhorn below Spitskopf formation, Schwarzrand subgroup; Saylor & Grotzinger, 1996), here named Nama, yielded lower intercept ages of 539.8±7.3 Ma (MSWD=1.8). This is within uncertainty identical to the U-Pb zircon age of 543±1 Ma from an ash layer of the Spitskopf formation (Bowring et al., 1993).

Points of each sample data set derived from a small area (<1 cm²) and defining linear arrays in the ²⁰⁷Pb/²⁰⁶Pb vs ²³⁸U/²⁰⁶Pb space (Tera-Wasserburg diagram) are interpreted to be a mixture of initial common-Pb and Pb that formed due to in situ decay of U since mineralization. The age of formation is defined by the lower intercept with the Concordia curve. Plots and ages were calculated using Isoplot 3.71 (Ludwig, 2007). All uncertainties are reported at the 2σ level.

3.4 Cyclostratigraphy

All cyclostratigraphic and statistical calculations were carried out using the Astrochron package for R (Meyers, 2014), if not stated differently, and are presented for the entire succession and in shorter segments. The proxy records were prepared prior to cyclostratigraphic analyses to remove long-term trends and to reduce non-

stationary variance. In case of analyses spanning the entire succession, outliers were removed first from the $\delta^{13}\text{C}$ record, and subsequently the records of water level and $\delta^{13}\text{C}$ were detrended with a LOESS regression ($f=0.3$, PAST 3.14, Hammer et al., 2001). Average spectral misfit (ASM) calculations and evolutive spectra (EHA) are based on these two records to estimate and track the sedimentation rate of the succession (Meyers & Sageman, 2007; Meyers et al., 2012). In this process, orbital target frequencies and their uncertainties were assessed for the Middle Miocene following the approach of Malinverno et al. (2010) as recommended by Meyers et al. (2012). The following procedures were applied prior to spectral analysis of shorter segments: CaSO_4 : (i) log-transformation, (ii) detrending with a LOWESS regression ($f=0.4$). $\delta^{13}\text{C}$: (i) removal of outliers, (ii) detrending with a LOWESS regression ($f=0.6$). Each record was linearly interpolated to obtain evenly spaced records. Initial data treatment was not required for the evenly spaced water level record (no long-term trend). Redfit spectra (Schulz & Mudelsee, 2002) were calculated with PAST 3.14 (Hammer et al., 2001) using a triangle (CaSO_4 record), or a rectangle window (records of $\delta^{13}\text{C}$ and water level). Gaussian band pass filtering was used to determine cycles from the proxy records and the astronomical solution for orbital tuning (Laskar et al., 2004). An EHA spectrum of the CaSO_4 record was calculated to evaluate sedimentation rate changes.

4. RESULTS

4.1 Results from laser ablation U-Pb dating

Laser ablation U-Pb dating was performed on thin sections of four samples, taken along the studied succession. Laser ablation spots in sample KL89 (wet saline mudflat, 118.84 m) were distributed in the calcareous matrix along the margins of anhydrite nodules. The remaining three samples consist of lacustrine limestones. In samples LAM (laminated mudstone, 289.25 m) and ORB330.85 (charophyte-debris packstone, 330.85 m), ablation spots were spread randomly, avoiding layers of silt-sized detrital

silicate. In sample GG2 (348.72 m), a microbial limestone with charophyte fragments, laser ablation spots are placed in the microbial matrix and in the cements inside the charophytes.

The resulting ages are 14.5 ± 1.5 Ma (KL89, MSWD=1.03, N=57), 12.1 ± 3.0 Ma (LAM, MSWD=0.70, N=55), 12.3 ± 1.5 Ma (ORB330.85, MSWD=1.19, N=51), 11.15 ± 0.33 Ma (GG2_matrix, MSWD=1.05, N=56), and 11.51 ± 0.59 Ma (GG2_cements, MSWD=0.63, N=37). Tera Wasserburg plots of the analyses are shown in Figure S1 (supplementary information).

4.2 Proxy records

Cyclostratigraphy and orbital tuning is based on records of CaSO_4 content, carbon isotope ratios and facies-derived water levels, whereas the records of oxygen isotope ratios and facies-derived salinities serve as independent paleoclimate proxies (Fig. 3).

The facies-derived records of water level and salinity follow the semi-quantitative (ground)water level and salinity dependent facies model of the Aktau succession established in Frisch et al. (2019). Sedimentary, lithological and mineralogical properties of the deposits were evaluated along detailed lithological logs at increments of 25 cm to assign a distinct stage of water level and salinity to each data point in accordance with the facies model. The water level record comprises six different levels of water availability, from distal alluvial fan to profundal lake environments. The main criteria for the definition of water levels in Frisch et al. (2019) were: (i) the amount and grain size of clastic input (proximal vs. distal deposition), (ii) indicators for the sediment drainage and position of the groundwater table (sediment color and mottling, desiccation cracks, rhizoliths, bedded or massive intra-sediment evaporites), and (iii) indicators for the persistence and depth of water coverage by lakes (occurrences of fossils, carbonaceous horizons, bedding or lamination, and type of subaqueous evaporites). The salinity record was deduced from the presence and

mineralogy of evaporites, tracking qualitative changes in alkalinity/salinity of the lake water and interstitial fluids (Frisch et al., 2019). Since there is no evidence for a direct influence of tectonics (e.g. the progradation of proximal alluvial fans in response to mountain uplift) on the water level and salinity records, these proxies are thought to reflect climatically forced changes in the hydrological budget of the endorheic basin (Frisch et al., 2019). Low water levels and high salinities are inferred to correspond to negative water budgets and vice versa. Facies analysis also revealed the evolution of the depositional environment from recharge playa, to discharge playa, to perennial lake, to intermittent lake (Fig. 3). A series of prominent marker horizons outline prominent changes in the depositional environment (MH1 to MH6; Figs. 1b, c and 3; Frisch et al., 2019). Additionally, MH0 is defined as a horizon of pronounced arid soil formation.

The water level record shows only moderate variations centered around dry mudflat conditions, until ~110 m. Further up, the water level increased and indicates perennial lacustrine conditions between about 190 and 260 m. After the progradation of proximal facies belts at ~260 m and the establishment of a low basin relief, the record exhibits high amplitude variations in a period characterised by the intermittent occurrence of lakes in an overall marginal lake setting.

The salinity record is characterised by low salinities in the recharge playa setting, whereas with the beginning of the discharge playa, evaporation drove salinities up to a prolonged period of anhydrite precipitation at MH3. With ongoing lake expansion, salinities decreased to on average alkaline lake conditions until MH5. Afterwards recurring periods of lake flooding and desiccation caused salinity variations between freshwater/alkaline conditions and gypsum saturation.

Regarding the endorheic setting of the Miocene Ili Basin, a strong correlation of water level and salinity record might be expected, which is not observed throughout the entire Aktau succession. The deep groundwater table of the recharge playa prevented evaporative water loss, wherefore changes in the basin hydrology were recorded only

by the water level record. The shallow groundwater table during the discharge playa phase enabled substantial evaporative loss, which resulted in high salinities but simultaneously limited further water accumulation and dampened water level fluctuations by high potential evaporation rates. The perennial lake facies did not allow a clear covariation of both parameters, since the overall high total water volume and the distal deposition restricted the sensitivity of facies variations in response to hydrological changes. A close coupling of water level and salinity was achieved in the intermittent lake facies due to the low basin relief and the overall marginal lake deposition, allowing for large lateral shifts of facies belts and a high sensitivity of both parameters towards the basin's hydrology.

The CaSO_4 record is related to the gypsum and anhydrite content of samples and indicates the onset and termination of discharge playa-type sedimentation between ~60 and ~190 m, featuring recurring cycles of flooding and desiccation. Peaks in the CaSO_4 content are mainly associated with interstitial sulphates of gypcrete deposits and layers of subaqueous evaporites with CaSO_4 contents up to 73% (82.9 m) and outline periods of high evaporation, accompanied by a negative water budget and solute concentration. Low CaSO_4 contents, usually close to 0%, are related to periods of enhanced aquifer recharge which caused lake and groundwater freshening. The exceptional coincidence of high water level and a first peak in gypsum content at MH1 is owed to the facies transition to the discharge playa setting. Coming from an overall dry environment, gypsum precipitation requires an initial pulse of higher water availability to grant solute supply and sufficient evaporation (Dupont-Nivet et al., 2007).

The carbonate stable isotope record encompasses pedogenic, phreatic and lacustrine carbonates. In case of lacustrine carbonates, the isotopic composition is mainly controlled by the balance of light meteoric waters and heavier, evaporative enriched lake- and groundwaters in the carbonate precipitating fluid (Li & Ku, 1997; Leng & Marshall, 2004). Stable isotope data show a large variability, which is mainly

environment dependent. The carbonate content varies between 10 and 20% in the recharge and early discharge playa (0-90 m) when mudflat environments prevailed and carbonates were precipitated from soil- or groundwater. Up section, the carbonate content of the lacustrine environment ranges from 20 to 40%. However, the correlation of the carbonate content and stable isotope data is weak (correlation coefficients between 0.15 and 0.25).

The $\delta^{18}\text{O}$ values exhibit an overall variability of almost 15‰. From the base of the succession up to ~80 m, values remain stable around an average of -7‰ with occasional strong negative inflections down to -13‰, which correspond to sheet flood sandstones. Above ~80 m, the $\delta^{18}\text{O}$ increases with the successive development of discharge playa conditions, culminating in a horizon with $\delta^{18}\text{O}$ values up to +1.8‰ between about 125 and 140 m. This increase is punctuated by two large and sudden enrichments by 6 ‰ at ~80 m and 4 ‰ at ~118 m. Above ~140 m, the oxygen isotope record displays a long-term trend towards lighter values, ending at ~260 m where the values decrease abruptly accompanied by lake siltation. From this point onwards, rhythmical short- and long-term variations with minima of about -13‰ and maxima around -1‰ can be observed.

The $\delta^{13}\text{C}$ record covers a range of ~13‰ and shows the highest variability at the base of the succession. After the absolute minimum of -13.2‰ at 9.0 m (sheet flood sandstone), $\delta^{13}\text{C}$ values increase up to -0.4‰ at 82.9 m (gypcrete horizon). In the lower Koktal Fm, a horizon between about 115.0 and 130.0 m is characterized by constantly high values up to -0.5‰. From the upper Koktal Fm upwards, the high frequency variations are dampened and a clear low frequency variation can be observed during the perennial lake phase. At the transition to the intermittent lake facies above ~260 m, $\delta^{13}\text{C}$ decreased by ~2‰. The absolute maximum of -0.1‰ is reached at 293.2 m in gypsiferous sediments, representing lake desiccation in the upper Kokterek Fm, where variations with short wavelengths are amplified again.

In hydrologically closed basins, a heavier carbon isotope composition of authigenic lacustrine carbonates is characteristic for a negative water budget at times of high evaporation ($\delta^{13}\text{C}$ maxima), whereas shifts towards lighter values reflect increased influxes of meteoric waters ($\delta^{13}\text{C}$ minima) (Li & Ku, 1997; Leng & Marshall, 2004). A terminal lake setting can be assumed based on the strong covariation of $\delta^{13}\text{C}$ and $\delta^{18}\text{O}$ values with (Pearson) correlation coefficients higher than 0.6 above MH4 (Talbot, 1990, Fig. 3). The carbon isotope record has been used for orbital tuning only in lacustrine environments because its variability is exclusively related to changes in lake water chemistry (lake recharge versus evaporation) and not related to the effects of phreatic and pedogenic carbonate formation, so that the proxy responds particularly sensitively to changes in the hydrological budget.

4.3 Facies dependent response of climatically forced proxy records

It was found that changes in the depositional environment are mainly climatically induced based on the result from facies analysis (Frisch et al., 2019). This study investigates the hypothesis that orbital forcing caused climate fluctuations and led to variations in the basin's hydrological budget, which were eventually recorded by the sedimentary facies and the geochemical proxies. Various studies have shown that orbital forcing controls the hydrological budget of endorheic basins, reflected by sedimentary cycles (Abdul Aziz et al., 2003; Abels et al., 2009; 2010; Mandic et al., 2011; Liu et al., 2014; Valero et al., 2014). In the Aktau succession, recurring evaporite formation in an overall arid to semi-arid climate setting suggests that the water budget was primarily controlled by evaporation, which is strongly dependent on temperature. Thus, insolation changes on Milankovitch time-scales seem a reasonable driver for variabilities in the hydrological budget. However, the proxy records show their maximum sensitivity towards climate forcing in different sedimentary environments.

For orbital tuning, the Aktau succession is split into four segments (I to IV) according to the boundaries of the four main facies zones to overcome the facies dependent climate sensitivity by choosing the most climate-sensitive proxy for each segment (Fig. 3). The recharge playa setting is represented by segment I. Attempts to improve the magnetostratigraphic age control by orbital tuning of a proxy record in segment I were not successful, and therefore the plain magnetostratigraphy (Table S1) defines the age model in segment I. The salinity-related CaSO_4 proxy is most suitable to reflect changes in the water budget in the discharge playa (segment II) due to the high control of the evaporation on the hydrological budget in this setting. The CaSO_4 record is preferred over the facies-related salinity, since the latter comprises only four semi-quantitative stages and does not allow an exact tracking of sedimentary cycles. The $\delta^{13}\text{C}$ signal of lacustrine carbonates shows the most sensitive response to hydrological changes during the lacustrine phase (segment III), since the depositional environment compromised the use of facies- and evaporite-related parameters. High amplitude variations render the water level record the most convenient proxy of water budget variability in the intermittent lake setting (segment IV), also because it comprises more gradations than the salinity record. The four segments overlap to check for consistency between the single parameters.

4.4 Estimation of sedimentation rate

Verestek et al. (2018) determined the position of seven magnetic polarity zone boundaries (chrons C5Bn.2n to C5ACn) between 12.5 m and 80.8 m spanning a period of 1.09 Ma from 15.160 Ma to 14.070 Ma (Table S1). Accordingly, an average sedimentation rate of 6.3 cm ka^{-1} can be assumed for segment I and the lowermost part of segment II. Above 80.8 m, the mean sedimentation rate is estimated to range between 8.2 and 10.3 cm ka^{-1} based on the more precise U-Pb age ($11.15 \pm 0.33 \text{ Ma}$) out of the two measurements available at 348.7 m, which is consistent with biostratigraphic evidence (Voigt et al., 2017).

ASM calculations and cycle frequency ratios deduced from redfit and EHA spectra for the Aktau succession above 80 m support these sedimentation rate estimates (Fig. 4a). The $\delta^{13}\text{C}$ redfit spectrum shows significant power (>90% chi square significance level) between wavelengths of 55 to 73 m, 31 to 38 m and in several peaks with wavelengths ranging from 5.5 to 8.7 m, 3.4 to 4.0 m and 2.0 to 2.6 m. The EHA spectrum reveals, that the 31 to 38 m, the 8.7 m and the 3.4 to 4.0 m cycles are well-developed and co-occur between approximately 100 and 200 m, exhibiting a ratio of 1:4.0:9.3 (calculated from the mean of wavelength ranges), which is close to the idealized theoretical value of 1:4:10 for the ratio of long to short eccentricity to obliquity. Thus, the continuous 31 to 38 m cycle likely represents the sedimentary expression of long eccentricity forcing above 80 m. The very long wavelength of 55-73 m appears only as one high amplitude oscillation between ~270 and 330 m and cannot be reliably detected throughout the record. This long-period variability is therefore not considered as a re-occurring cycle and excluded from further investigations.

The water level record exhibits significant power (>90% chi square significance level) in the redfit spectrum between 36 and 73 m, at 10.9 m, around 8.6 m, between 4.7 and 5.2 m and in a series of peaks from 1.6 to 2.8 m. The 36-73 m wavelengths appear with high amplitudes in the EHA spectrum especially above ~150 m together with the 10.9 m, ~8.7 m and 4.7 to 5.2 m wavelengths, whereas the latter appear to be less steady. In contrast to the $\delta^{13}\text{C}$ record, where the redfit spectrum exhibits two distinct peaks for the significant 55-73 m and the 31-38 m wavelengths, these wavelengths are merged in one peak in the redfit spectrum of the water level due to low signal sensitivity. The calculation of the ASM metric for both parameters above 80 m (Fig. 4b) confirms that the power spectra of $\delta^{13}\text{C}$ and water level reflect orbital forcing for sedimentation rates around 10 cm ka^{-1} ($\delta^{13}\text{C}$: 9.6 to 10.0 cm ka^{-1} , water level: 10.4 to 10.7 cm ka^{-1} , Fig. 4b, and c), in close agreement with the estimate from U-Pb dating. Higher sedimentation rates after the transition from recharge to discharge playa is also evident in the evolutive spectra of $\delta^{13}\text{C}$ and water level (Fig. 4a). Both spectra show significant and high

amplitudes at wavelengths of around 20 m below ~100 m thickness, whereas above, this dominant cyclicity shifts to wavelengths of around 30 to 40 m. To conclude, sedimentation rate estimates for the Aktau succession above 80 m support the notion that the prominent 31 to 38 m wavelength represents the imprint of long eccentricity forcing. The match of target and candidate frequencies at the most likely average sedimentation rate (Fig. 4c) reveals deviations in case of short eccentricity, obliquity and precession, which may be explained by variations of the sedimentation rate on shorter timescales. The unsteady behaviour of the interpreted short eccentricity and obliquity wavelengths in the EHA spectra along the entire succession points to signal distortion by non-linear feedbacks of the proxy records to climate forcing, transferring power from short to long periodicities (Liebrand et al., 2017). The rather stable long eccentricity signal is stabilized by the increased influence of the more steady basin subsidence on sedimentation on longer timescales. The non-linearities in the short-term sedimentary response are mainly related to unstable sedimentation rates because of periods of non-deposition or erosion at low water levels caused by cycles of flooding and desiccation in segments II and IV. This resulted in preferentially condensed sedimentary expressions of short orbital cycles and a poor match with long eccentricity related wavelengths.

4.5 Redfit and EHA spectra for segments II to IV

Redfit power spectra for each parameter in segments II to IV are presented in Figure 5a. Significant peaks (>90% chi-square significance level) are labelled with their interpreted orbital component based on the sedimentation rate estimates outlined in the previous section. In segment II, the abovementioned variations in sedimentation rate are expressed by the splitting of the low frequency peak with significant wavelengths ranging from 25 to 27 m and from 39 to 49 m, which reflects the imprint long eccentricity. The wavelengths of 6.5 to 6.9 m possibly corresponds to short

eccentricity forcing at times of low sedimentation rates in accordance with the long eccentricity candidate cycle encompassing wavelengths from 25 to 27 m.

The EHA spectrum of segment II shows a change in the wavelength of the short eccentricity-related cycle associated with an increase in sedimentation rates between ~75 m and ~100 m. Wavelengths of about 7 m at ~70 m increase to ~12 m between 100 and 130 m and decrease again to ~7 m above ~130 m. These shifts are accompanied by similar changes in the wavelength of the long eccentricity imprint (Figure 5b). Accordingly, the sedimentary expression of the long eccentricity cycle features a longer wavelength (spectral peak from 39 to 49 m) in the lower part (approximately 100 to 130 m) of segment II and a shorter wavelength (spectral peak from 25 to 27 m) in the upper part (above ~130 m).

Bandpass filter outputs (centered at 48 m and 26 m) show that the number of short eccentricity-related cycles (CaSO_4 peaks) matches the length of the filtered long eccentricity cycle between ~130 m and 190 m (Fig. 5b). Additionally, high amplitude peaks form bundles of two or three within one long eccentricity-related filter output maxima, resembling the pattern of precession amplitude modulation by eccentricity. However, the identification of short eccentricity cycles in the interval of higher sedimentation rates remains ambiguous.

The assignment of higher frequency spectral peaks (wavelengths of ~5.2 m, 4.3 to 4.4 m, 3.2 to 3.5 m and shorter) to orbital cycles in segment II is hindered by the cycle frequency ratio distortion due to facies-related discontinuous sedimentation.

In segment III, strong spectral power for wavelengths between 31 and 57 m probably represents forcing by long eccentricity. In segment IV, spectral peaks with wavelengths between 35 to 45 m are assigned to long eccentricity, a double peak around wavelengths of 8.7 and 10.9 m resembles the imprint of short eccentricity, a cycle length of 4.6 m is a likely candidate for obliquity forcing, and several significant peaks of wavelengths from 1.4 to 2.0 m tentatively correspond to precession forcing.

The corresponding wavelength ratio of 1:4:9:23 (wavelength ranges averaged) is close to the Milankovitch periodicities (long to short eccentricity, to obliquity, to precession). An investigation of higher frequency peaks in segment IV seems possible, since the water level record has a higher resolution than the geochemical proxies. However the potential precession cycles are generally weakly developed and discontinuous as evident from the water level EHA spectrum in segment IV (Fig. 4a), wherefore an autogenic origin of these cycles must be considered (cf. Trampush et al., 2017).

4.6 Band-pass filtering and orbital tuning

In segments III and IV, the interpreted expression of the long eccentricity cycle was band-pass filtered from the parameters according to the cycle lengths given by the redfit spectra, which resulted in filters of 38 m ($\delta^{13}\text{C}$ record) and 40 m (water level record).

The magnetostratigraphy constrains the minimum in the 48 m filter of the CaSO_4 record at ~75 m to the long eccentricity minimum at 14.180 Ma of the astronomical solution (Fig. 6). From this point on, consecutive in-phase tuning of filter minima and maxima to the astronomical target cycle was maintained in segment II. This phase relation, corroborated by the observed eccentricity amplitude modulation pattern of the CaSO_4 record, suggest that higher insolation during eccentricity maxima coincided with high CaSO_4 deposition, likely through high evaporative brine concentrations. The overlap of the minima in the 48 m and the 26 m CaSO_4 filter curves at ~122 m is used to switch to the 26 m CaSO_4 filter to account for lower sedimentation rates (Fig. 6).

Within the overlap of segments II and III, the 26 m filter of the CaSO_4 record and the 38 m filter of the $\delta^{13}\text{C}$ run in phase and show a maximum at ~187 m (Fig. 6). This maximum was used to change to the $\delta^{13}\text{C}$ record of segment III, adopting the same

phase relation. The same phase relation of CaSO_4 and $\delta^{13}\text{C}$ to the tuning target is plausible as both records are controlled by the balance of evaporative water loss (higher $\delta^{13}\text{C}$ and CaSO_4 content) and dilution by meteoric water recharge (lower $\delta^{13}\text{C}$ and CaSO_4 content). Consecutive orbital tuning continues until the maximum of the 38 m $\delta^{13}\text{C}$ filter at ~252 m.

In segment IV, we assume that enhanced evaporation due to higher insolation and diminished aquifer recharge because of strong climate seasonality resulted in low water levels during eccentricity maxima. A continuing strong control of evaporation on the water budget is suggested by the re-occurrence of evaporites in segment IV. This phase relation is supported by the 1.6 m filter output of the water level record, which was tentatively interpreted to express the imprint of precession, thereby showing periods of high (low) amplitudes coeval to minima (maxima) of the 40 m filter of the water level record (Fig. 6). This pattern would confirm that minima of the 40 m filter correspond to maxima of the 405 ka target cycle, since precession cycles have a larger amplitude at high eccentricity. This phase relationship of the 40 m filter and the target cycle seemingly calls for an inversely phased tuning.

Within the overlap of segment III and IV, the facies change from perennial to intermittent lacustrine conditions started at ~260 m, expressed by lake siltation and progradation of proximal facies. This facies change is accompanied by soil formation at ~264 m. This implies the occurrence of a pedogenic signal in the $\delta^{13}\text{C}$ record of segment III, which would lead to spurious cyclostratigraphic inferences. Therefore, no tie points are placed from 260 to 280 m. The next tie point is defined by the maximum of the 40 m water level filter at 295.0 m, which is assigned to the long eccentricity minimum at 11.345 Ma (Fig. 6). Tuning of this filter maximum to the target cycle minimum at 11.750 Ma would result in unrealistically high sedimentation rates. Tie points for the proposed age model and their tuning targets are given in Table S2.

5. DISCUSSION

5.1 Age model

The age model for the Aktau succession integrates the results of cyclostratigraphy, magnetostratigraphy and laser ablation U-Pb dating (Fig. 7). The cyclostratigraphic age model lies within the uncertainty range of the U-Pb ages of samples KL89, LAM, and ORB330.85. In case of sample GG2, both U-Pb ages exhibit slightly older ages compared to the cyclostratigraphic age model (Fig. 7). The offset can be explained by the presence of dispersed fine-grained Paleozoic detritus in the carbonates, which could not be avoided by the choice of laser ablation spots. The increased uncertainty of filtered tie point positions near the end of a time series likely compensates this offset, since a shift of only 1.6 m of the tie point at 355.25 m is needed to close the 10 ka gap to the youngest possible age for sample GG2_matrix.

The overall uncertainty of the cyclostratigraphic age model is estimated to be smaller than 100 ka in segments II and III, with highest uncertainties at times of changing sedimentation rate (early segment II). Above ~280 m, the uncertainty is estimated to be in the order of half a 405 ka eccentricity cycle.

Relatively low and stable sedimentation rates of the Aktau succession (5.8 to 12.2 cm ka⁻¹) support the assumption of steady but low tectonic activity during the Middle Miocene in the Ili Basin (Frisch et al., 2019). Together with the closed basin configuration, sedimentation was largely controlled by the regional hydrological budget and base level changes. High water availability is accompanied by higher sedimentation rates (from ~200 m onwards) due to the enhanced precipitation of authigenic minerals, i.e. carbonate in lacustrine environments (Fig. 7). Contrarily, sedimentation in the recharge and discharge playa environments was condensed due to frequent desiccation events (Fig. 7). Relatively high sedimentation rates between 90 and 130 m (11.2 to 12.2 cm ka⁻¹, Fig. 7) are also reflected in the preservation of laminated pedogenic gypsum (Frisch et al., 2019).

5.2 Eccentricity forcing

Numerous studies of Miocene to Pliocene peri-Mediterranean lakes argue for positive water budgets due to enhanced (winter) precipitation at times of maximum insolation on a precession scale in analogy to the climatic mode for sapropel formation (van Vugt et al., 1998; Abdul Aziz et al., 2003; Abels et al., 2009; Mandic et al., 2011). The opposite relation, with negative water budgets resulting in evaporite formation during precession driven insolation maxima, was suggested for the Eocene Lake Gosiute, Green River Formation, USA (Morrill et al., 2001; Smith et al., 2014). Although precession is the main carrier of insolation variations (Hilgen et al., 2015), precession and in part also short eccentricity cycles are weakly developed in the Aktau succession. This is mainly related to (i) nonlinearities in the climatic and sedimentary response to orbital forcing, which cause signal distortion by variations in sedimentation rate (Hilgen et al., 2015), and (ii) a dampening of the high frequency precession forcing by the size-dependent sluggish response of the lake and groundwater aquifer. Results of this study show a strong impact on the hydrology of the closed Ili Basin by the long eccentricity cycle, which was recorded in the sedimentary archive by eccentricity modulated precession. The 405 ka cycle is a stable component of all studied time series, since its relatively long periodicity minimized signal distortion by aquifer lag time and short-termed non-linear responses by allowing a strong control of the steady basin subsidence on the deposition.

Phase relations of the proxy records, independently constrained by magnetostratigraphy, laser ablation U-Pb dating and amplitude modulation patterns, suggest a correlation of negative water budgets with high eccentricity. Given the arid to semi-arid climate regime and the absence of substantial fluvial discharge, the balance of evaporation and subsurface aquifer recharge is considered the most sensitive control on the hydrological budget, in response to eccentricity modulated insolation changes. Consequently, negative water budgets during 405 ka eccentricity

cycle maxima, were caused by high amplitudes of eccentricity modulated precession with recurring periods of high potential evapotranspiration and extreme seasonality of precipitation, promoting lowered recharge rates, lake contraction and salinization. This is underlined by the bundling of high amplitude short-eccentricity cycles in the CaSO_4 record (Fig. 5). Conversely, positive water budgets with lake expansion and lake- and groundwater freshening characterize 405 ka eccentricity minima when aquifer recharge was facilitated by low precession amplitudes. Thus, the long-term presence/absence of strong precessional climate forcing is responsible for negative/positive water budgets, which explains the imprint of the 405 ka cycle in the sedimentary record (cf. Abels et al., 2010). These findings are contrary to the phase relationship of the 405 ka cycle reported for Miocene lakes in southern Europe, where lake highstands coincide with eccentricity maxima (Abdul Aziz et al., 2003; Abels et al., 2009, 2010; Mandic et al., 2011; Valero et al., 2014). The Middle Miocene climate in southern Europe, with mean annual precipitation values between 500 and 1000 mm (Bruch et al., 2011; Böhme et al., 2011), was more humid than the semi-arid to arid basins in Central Asia. Here, we hypothesize that the phase relation between long eccentricity and water availability depends on the total amount of annual moisture availability, which controls the relative forcing dominance of the factors evaporation and precipitation on the water budget.

The hydrological evolution of the Aktau succession is also influenced by the very long 2.0-2.8 Ma eccentricity cycle as the pacemaker for long-term changes in the depositional environment. Minima of the 2.4 Ma cycle have previously been linked to water level highstands in alluvial-lacustrine settings and to proliferation of wet-adapted mammals because of a long-term absence of extreme evaporation (Abels et al., 2009, 2010; van Dam et al., 2006). This notion is supported by the observations from the Aktau succession, where long-term eccentricity minima promoted the accumulation of groundwater and the establishment of the discharge playa-type sedimentation (~14.3 Ma) and drove the expansion of the perennial lake (12.6-11.8 Ma,

Fig. 8). Altogether, the sensitivity to eccentricity modulated precession, observed in the sedimentary Aktau succession, is in agreement with an overall eccentricity dominated global climate during the Middle and early Late Miocene, as deduced from benthic $\delta^{18}\text{O}$ deep-sea records (Holbourn et al., 2013, De Vleeschouwer et al., 2017).

5.3 Long period obliquity forcing

Several periods of arid soil formation or pronounced lake- and groundwater salinization, at ~15.0 Ma, ~13.8 Ma, ~12.7 Ma and weakly also at ~11.3 Ma, coincide with the nodes of obliquity amplitude modulation (Fig. 8). This is consistent with findings of van Dam et al. (2006), who observed more arid conditions during obliquity nodes in Neogene sediments from Spain. Conversely, periods of freshening of lake and ground waters match periods of high amplitude modulation of obliquity. Here, we propose obliquity-driven changes in the westerly wind strength as the main process responsible for the amount of atmospheric moisture transported to Central Asia.

The westerlies, today the main moisture carrier to Central Asia, were likely active in the study area since the Eocene (Caves et al., 2015; Licht et al., 2016; Caves Rugenstein & Chamberlain, 2018). The strength of the westerlies is affected by the meridional insolation gradient, which is controlled by the Earth's tilt angle (Mantsis et al., 2011, 2014). Particularly low tilt angles at times of high obliquity amplitudes increase the meridional insolation gradient especially in summer. This enhances the overall atmospheric circulation, leading to a strengthening of the mid-latitude westerly winds together with an equatorward shift of the descending branch of the Hadley cell (Mantsis et al., 2011, 2014). Enhanced westerlies are assumed to deliver more atmospheric moisture to Central Asia, which resulted in a long-term water accumulation, brine dilution and more surface discharge at times of maximum obliquity amplitudes. Conversely, obliquity nodes, which lack extremely low tilt

angles, correspond to diminished westerly intensities, which reduced atmospheric moisture supply and facilitated lake and groundwater salinization.

Obliquity forcing in the Aktau succession, with a most sensitive response of salinity to obliquity amplitude modulation around the obliquity node of ~13.6 Ma, matches the history of obliquity forcing of global climate, as observed in deep-sea records. The salinization of the Ili Basin concomitant to a period of enhanced obliquity (41 ka) forcing between ~14.6 and 13.8 Ma (Holbourn et al., 2013, 2014) likely reflects the increased influence of the westerly wind dynamics on the hydrological budget. Additionally, Levy et al. (2019) argued for an elevated sensitivity of global climate to obliquity forcing between ~15.0 and 13.5 Ma via Antarctic ice sheet dynamics.

5.4 Hydrological evolution of the Ili Basin

The Aktau succession records almost five million years of climate-driven changes in regional hydrology between 15.6 Ma and 10.6 Ma covering the late MCO and the MCT (Fig. 8). The most prominent feature of the Aktau succession is an overall increase in water availability from dry to wet mudflat to lacustrine conditions. According to the definitions of endorheic basin hydrology by Rosen (1994), the Ili Basin changed from a recharge playa between 15.6 and ~14.3 Ma to a discharge playa afterwards. In discharge playas, the balance of potential evaporation in the arid to semi-arid basin centre and recharge by precipitation in the surrounding mountains of the catchment area determines the hydrological budget (Rosen, 1994). This is well-demonstrated by the oxygen isotope record, which reflects the isotopic fractionation and thus the degree of salinization determined by the ratio of evaporation and precipitation.

Until ~14.3 Ma (MH1) oxygen isotope values around -7‰ are characteristic for pedogenic and/or vadose formation of carbonates above the groundwater table in a dry mudflat. The sudden negative isotope excursions are related to sheet floods and represent the cementation of the pore space by carbonate precipitated from meteoric

water (Voigt et al., 2017). Ephemeral positive $\delta^{18}\text{O}$ excursions (e.g. at ~14.9 Ma, MH0) occurred due to ponding of flood water and subsequent evaporative isotopic enrichment. The onset of recurring gypsum precipitation at ~14.3 Ma (MH1) was facilitated by the first-time occurrence of palustrine conditions, when increased aquifer recharge and a higher groundwater table enabled substantial evaporative capillary groundwater rise. A sudden 6‰ increase in oxygen isotopes is related to the formation of massive gypcrete beds, enabled by higher evaporation rates due to the first-time occurrence of a permanently shallow groundwater table, ensuring full interaction of the atmosphere and the aquifer and indicating the ultimate establishment of discharge playa conditions at ~14.1 Ma (MH2).

The period between ~13.7 and 13.5 Ma (MH3) represents the time of highest evaporation rates in the Ili Basin initiated at ~13.8 Ma by a second abrupt 4‰ increase of oxygen isotopes, after a minor increase of the water level at ~13.9 Ma. Between ~13.5 and 11.8 Ma, the ratio of evaporation and recharge by precipitation reversed and a progressively positive water budget led to brine dilution and lake expansion with a continuous long-term decrease in the oxygen isotope record. Another short episode of severe drought occurred at ~12.7 Ma (MH4), when a transient negative water budget increased lake salinities until complete desiccation demonstrated by a prominent $\delta^{18}\text{O}$ peak. Afterwards, a perennial lake persisted for ~800 ka between 12.6 and 11.8 Ma. In response to lake level retreat at ~11.8 Ma (MH5) the oxygen isotope values markedly decreased and remained low until ~11.6 Ma, indicating the formation of carbonates from meteoric waters by enhanced surface run-off. Subsequently, alternations of positive and negative water budgets resulted in lake expansion and contraction, the latter provoking gypsum precipitation. Lake siltation occurred again at ~10.8 Ma (MH6) followed by a period of negative water budgets and prolonged evaporite formation.

Interestingly, there seems to be a coincidence in the timing of hydrology changes in the Ili Basin and oceanographic changes in the Paratethys. The period of highest

evaporation rates (~13.7 to 13.5 Ma) occurred simultaneously to the Badenian Salinity Crisis in the Central Paratethys and the isolation of the Eastern Paratethys during the Karaganian (de Leeuw et al., 2010, 2018; Palcu et al., 2017). Moreover, the interval of maximum lake expansion (~12.6 to 11.8 Ma) coincided with the reunification of the Paratethys after the Konkian-Volhynian boundary (Palcu et al., 2017). Further regional-scale research is needed to assess what kind of climatic processes linked changes in the two depositional systems.

5.5 Basin hydrology in context of the MCT

Milestones in the basin's hydrological evolution coincide with the timing of global climatic changes during the MCT. Groundwater accumulation and salinization commenced with the onset of the MCT and Antarctic glaciation after ~14.6 Ma (Shevenell et al., 2004, 2008; Holbourn et al., 2013, 2014) and progressed until the main cooling event Mi3b at 13.8 Ma (Abels et al., 2005; Westerhold et al., 2005; Holbourn et al., 2013). The salinization trend in the Ili Basin is more similar to the gradual $\delta^{18}\text{O}$ (benthic) increase found in the Mediterranean during this interval, than to the abrupt Mi3b $\delta^{18}\text{O}$ (benthic) shift recorded in the South China Sea (Fig. 8, Mourik et al., 2011; Holbourn et al., 2013). Highest evaporation rates from 13.7 to 13.5 Ma are promoted by the co-occurrence of long eccentricity maximum and obliquity node. A stronger influence of obliquity forcing on global climate (Levy et al., 2019) could have amplified the climatic effects of obliquity nodes and contributed to exceptionally high evaporation rates from ~13.7 to 13.5 Ma. Perennially positive water budgets occurred from ~12.7 Ma to 11.6 Ma, provoking lake expansion after 12.7 Ma. The onset of lake expansion occurred simultaneous to climate cooling of Mi4 (13.2 to 12.8 Ma, Westerhold et al., 2005; Holbourn et al., 2013) and perennial lacustrine conditions were recorded for the first time following the Mi4 cooling. These results argue for a causal relation between the water accumulation in the Ili Basin and the global cooling after the MCO (Zachos et al., 2001). Climate cooling influenced the water budget by altering

both factors evaporation and precipitation. Regional evaporation in the Ili Basin was likely lowered by globally decreasing temperatures, facilitating moisture condensation and limiting evaporative water loss. Additionally, precipitation in the catchment area was probably enhanced by intensified westerlies, eventually resulting in groundwater table rise and lake expansion.

5.6 Intensification of westerly winds during and after the MCT

Miocene water accumulation in the Ili Basin concurs with large-scale climatic patterns reported for western and south-western Eurasia and thus in areas located upwind along the westerlies' pathway. Lower but highly variable $\delta^{18}\text{O}$ (planktic) values indicate seasonally enhanced freshwater influx into the Mediterranean after 13.8 to 13.7 Ma (Mourik et al., 2011). In Central and Eastern Europe a relatively dry early Middle Miocene climate, was followed by drier conditions in the (Early) Serravallian and a successively wetter climate towards the Tortonian (van Dam, 2006; Bruch et al., 2011; Böhme et al., 2008, 2011). Increasing amounts of precipitation after 13.2 Ma, with peak values between 11 and 10.3 Ma, are reported for the Alborz Mountains, Northern Iran (Ballato et al., 2010). The European Temperate Wet Zone, developed following the early Middle Miocene drought with increasing precipitation after 13 Ma and showed its maximum extension between 12 and 9 Ma (van Dam, 2006). The more humid climate in the late Middle and early Late Miocene developed in the context of Northern Hemisphere cooling, which led to a southward retreat of the subtropical high-pressure belt giving way to a zonal circulation dominated by westerly winds (van Dam, 2006). Eronen et al. (2012) and Böhme et al. (2008) also suggest an increased cyclonic activity over Europe in the Tortonian. Northern Hemisphere cooling in the course of the MCT likely led to a stronger meridional temperature gradient, resulting in stronger westerly winds (cf. Routson et al., 2019). In addition, the onset of the South Asian Monsoon at 12.9 Ma (Gupta et al., 2015; Betzler et al., 2018) could have indirectly contributed to a stronger westerly jetstream over Central Asia. According to

Schiemann et al. (2009), a stronger than average modern Indian Summer Monsoon strengthens the westerly jetstream north of the Tibetan Plateau and keeps it in its northern position for a longer time during the year. To conclude, enhanced westerly-sourced precipitation in the Ili Basin's catchment area likely triggered the basin's salinization by raising the groundwater table under highly evaporative conditions after ~14.3 Ma and promoted the subsequent lake expansion after the reversal of the hydrological budget at ~13.3 Ma.

5.7 Tian Shan as climate boundary

Comparison to time equivalent records located east of the Tian Shan reveals a contrary development with intensified aridification after the Middle Miocene (Fig. 1a). In the southern Junggar Basin, progressive aridification took place after 16.2 Ma with constantly dry climate from 13.5 Ma onwards (Tang et al., 2011), which concurs with the onset of eolian sedimentation in the northern Junggar Basin at 13.5 Ma after a period of fluvio-lacustrine deposition (Sun, J. et al., 2010). Successions of the Junggar Basin studied by Charreau et al. (2012) yield Early and Middle Miocene lacustrine sediments, which are absent from the late Middle Miocene onwards. Similarly, the climate of the Tianshui Basin and the Lanzhou Basin at the north-eastern edge of the Tibetan Plateau was assumed to have been warm and humid from 17.1 to 14.7 Ma, respectively from 17.1 to 14.1 Ma and became substantially drier afterwards (Hui et al., 2011; Zhang, Y. et al., 2014). Evidence for a shift from humid to more arid conditions after 13.5 Ma comes from the hypsodonty patterns of Chinese herbivorous mammals (Liu et al., 2009). Records from the Qaidam Basin, NE Tibet propose substantial aridification from ~12 Ma onwards (Zhuang et al., 2011) and after 11.1 Ma (Song et al., 2014). In contrast, the Miocene Guide Basin in north-east Tibet exhibits highest lake levels between 11.4 and 10.5 Ma (Wang et al., 2018), and seems to follow the climate development of Western Eurasia and the Ili Basin. In this context, Wang et al. (2018, 2019) discuss a substantial moisture supply by the westerlies to the Miocene

Guide and Tianshui Basin, where lake level variations are predominantly eccentricity controlled. Contrary hypotheses exist about the Miocene hydroclimate of the Tarim Basin, south of the Ili Basin. Zheng et al. (2015) argue for aridification and desertification in response to the uplift of the Tibetan-Pamir Plateau and the Tian Shan at the Oligocene-Miocene boundary, whereas Sun et al. (2015, 2017) and Liu et al. (2014) propose more humid conditions with episodic lakes and westerly moisture supply via a narrow pathway between the Tian Shan and the Pamir until the Late Miocene. This hampers the comparison of Miocene hydroclimate trends from the Ili and Tarim Basin. However, the diverging paleoprecipitation patterns between the Ili Basin and its eastern vicinity suggests that the orogenic barrier effect of the initially uplifted Tian Shan became particularly pronounced once zonal westerly winds were enhanced after the MCT. This could explain the observed increase in westerly-related precipitation on the windward side of the Tian Shan (Ili Basin) coeval to drier conditions in leeward areas (i.e. the Junggar Basin). These observations support the notion that Central Asian mountain chains acted as climatic boundaries already in the Miocene (Caves et al., 2017).

6. SUMMARY AND CONCLUSIONS

The Aktau succession represents an exceptionally undisturbed Miocene paleoclimate archive in the otherwise tectonically active setting of Central Asia. From 15.6 to 10.6 Ma, the 5.0 Ma long succession recorded long-period orbital forcing as well as the impact of the Neogene global cooling after the Miocene Climatic Optimum (MCO) on the hydrological budget of the Ili Basin. The main conclusions are:

- 1 Recurring strong seasonality, forced by eccentricity modulated precession, caused the imprint of the 405 ka cyclicity on the basin hydrology. 405 ka eccentricity cycle maxima led to negative water budgets, resulting in low water levels, solute enrichment and evaporite formation. Periods of water accumulation and brine

dilution are coupled to 405 ka eccentricity cycle minima due to the long-term absence of extremely evaporative conditions. Similarly, positive water budgets during long-term eccentricity minima around ~14.3 and ~12.3 Ma triggered major environmental changes by initiating discharge playa conditions and the expansion of the perennial lake.

2 Repeated occurrence of extremely low tilt angles during maxima of the 1.2 Ma cycle of obliquity amplitude modulation led to a stronger meridional temperature gradient, enhancing the strength of the westerly winds and thereby favouring a long-term positive water budget by increasing precipitation in the catchment area. Conversely, obliquity nodes resulted in negative water budgets at ~15.0, ~13.7 to 13.4 Ma, ~12.7 Ma and at ~11.3 Ma due to diminished atmospheric moisture supply by weak westerlies.

3 The hydrological evolution of the Ili Basin developed in concert with global climate cooling after the MCO (Zachos et al., 2001). Distinct steps of groundwater accumulation and salinization at ~14.3 and ~14.1 Ma occurred coeval to the Miocene Climate Transition (MCT) onset and culminated with maximum evaporation rates after ~13.8 Ma, probably in response to climate feedbacks related to the major Antarctic ice sheet expansion (Holbourn et al., 2005). Progressive global climate cooling led to brine dilution and establishment of the perennial lake between ~12.6 and 11.8 Ma.

4 Groundwater accumulation and salinization is ascribed to enhanced precipitation in Central Asia by intensified westerly winds in response to Northern Hemisphere cooling. A sufficiently large aquifer enabled maximum evaporation rates after ~13.8 Ma. Positive water budgets after ~13.3 Ma resulted from a combination of declining evaporation rates and further moisture supply by stronger westerlies during and after the later stage of the MCT.

5 The Aktau record emphasizes the impact of global climate change and long-period orbital forcing on the strength of the westerlies and eventually on the hydrology of

the Central Asian Ili Basin during the Middle to Late Miocene. Regionally diverging precipitation patterns, resulting in lake expansion in the windward Ili Basin coeval to aridification in the neighbouring leeward basins, highlights the role of the Tian Shan as climatic boundary already in the Middle to Late Miocene.

ACKNOWLEDGEMENTS

We are grateful to our Kazakh cooperation partners S. Nigmatova, R. Sala and J.-M. Deom (Geological Institute K. Satpaeva, Almaty and University of Almaty). The administration and rangers of the State National Park Altyn Emel are thanked for providing access to the Aktau Mountains. We thank K. Kossov and J. Zhilkina for field logistics and their friendly company. An anonymous reviewer and Jeremy Caves Rugenstein are thanked for their insightful comments, which improved the quality of the manuscript. We thank H. Abels and F. Hilgen for their valuable comments on the cyclostratigraphy and the orbital tuning presented in this manuscript. A. Hellwig is thanked for lab work assistance. S. Hofmann and L. Marko provided technical support. This study was financed by DFG grants VO 687/16 and AP 34/41-1, additionally W. Frisch is thanked for financial support to K.F. The datasets of stable carbon and oxygen isotopes, CaSO_4 content and the laser ablation U-Pb dating presented in this study are available at <https://doi.pangaea.de/10.1594/PANGAEA.906094>

REFERENCES

Abdul Aziz, H., Krijgsman, W., Hilgen, F. J., Wilson, D. S., & Calvo, J. P. (2003). An astronomical polarity timescale for the late Middle Miocene based on cyclic continental sequences. *Journal of Geophysical Research*, 108(B3), 2159. <https://doi.org/10.1029/2002JB001818>

Abels, H. A., Abdul Aziz, H., Calvo, J. P., & Tuenter, E. (2009). Shallow lacustrine carbonate microfacies document orbitally paced lake-level history in the Miocene Teruel Basin (North-East Spain). *Sedimentology*, 56, 399–419. <https://doi.org/10.1111/j.1365-3091.2008.00976.x>

Abels, H. A., Abdul Aziz, H., Krijgsman, W., Smeets, S. J. B., & Hilgen, F. J. (2010). Long-period eccentricity control on sedimentary sequences in the continental Madrid Basin (Middle Miocene, Spain). *Earth and Planetary Science Letters*, 289, 220–231. <https://doi.org/10.1016/j.epsl.2009.11.011>

Abels, H. A., Hilgen, F. J., Krijgsman, W., Kruk, R. W., Raffi, I., Turco, E., & Zachariasse, W. J. (2005). Long-period orbital control on Middle Miocene global cooling: Integrated stratigraphy and astronomical tuning of the Blue Clay Formation on Malta. *Paleoceanography*, 20, PA4012. <https://doi.org/10.1029/2004PA001129>

Akhmetyev, M. A., Dodoniv, A. E., Sornikova, M. V., Spasskaya, I. I., Kremenetsky, K. V., & Klimanov, V. A. (2005). Kazakhstan and Central Asia (plains and foothills). In A. A. Velichko & V. P. Nechaev (Eds.), *Cenozoic climatic and environmental changes in Russia*, Geological Society of America Special Paper (Vol. 382, pp. 139–161).

Ballato, P., Mulch, A., Landgraf, A., Strecker, M. R., Dalconi, M. C., Friedrich, A., & Tabatabaei, S. H. (2010). Middle to late Miocene Middle Eastern climate from stable oxygen and carbon isotope data, southern Alborz mountains, N Iran. *Earth and Planetary Science Letters*, 300, 125–138. <https://doi.org/10.1016/j.epsl.2010.09.043>

Bazhanov, V. S., & Kostenko, N. N. (1961). Geologicheskii razrez Dzhungarskogo Alatau i ego paleozoologicheskoye obosnovanie [Geological section of Dzhungarian Alatau and its paleontological basis]. In I. G. Galuzo (Ed.), *Materialy po istorii fauny i flory Kazakhstana*, Akademia Nauk Kazakhskoy SSR (Vol. 3, pp. 47–52). Alma Ata.

Betzler, C., Eberli, G. P., Lüdmann, E., Reolid, J., Kroon, D., Reijmer, J. J. G., et al. (2018). Refinement of Miocene sea level and monsoon events from the sedimentary archives

of the Maldives (Indian Ocean). *Progress in Earth and Planetary Science*, 5(5).
<https://doi.org/10.1186/s40645-018-0165-x>

Bodina, L. E. (1961). Ostrakody tretichnykh otlozhenii Zaisanskoi I Iliiskoi depressii [Ostracods of Tertiary deposits in the Zaisan and Ili depressions]. *Trudy VNIGRI*, 170, 43–153.

Bosboom, R., Dupont-Nivet, G., Grothe, A., Brinkhuis, H., Villa, G., Mandic, O., et al. (2014). Timing, cause and impact of the Late Eocene stepwise sea retreat from the Tarim Basin (west China). *Palaeogeography, Palaeoclimatology, Palaeoecology*, 403, 101–118. <https://doi.org/10.1016/j.palaeo.2014.03.035>

Böhme, M., Ilg, A., & Winklhöfer, M. (2008). Late Miocene “washhouse” climate in Europe. *Earth and Planetary Science Letters*, 275, 393–401.
<https://doi.org/10.1016/j.epsl.2008.09.011>

Böhme, M., Winkelhofer, M., & Ilg, A. (2011). Miocene precipitation in Europe: Temporal trends and spatial gradients. *Palaeogeography, Palaeoclimatology, Palaeoecology*, 304, 212–218. <https://doi.org/10.1016/j.palaeo.2010.09.028>

Bougeois, L., Dupont-Nivet, G., de Rafélis, M., Tindall, J. C., Proust, J.-P., Reichert, G.-J., et al. (2018). Asian monsoons and aridification response to Paleogene sea retreat and Neogene westerly shielding indicated by seasonality in Paratethys oysters. *Earth and Planetary Science Letters*, 485, 99–110. <https://doi.org/10.1016/j.epsl.2017.12.036>

Bowring, S. A., Grotzinger, J. P., Isachsen, C. E., Knoll, A. H., Pelechary, S. M., & Kolosov, P. (1993). Calibrating rates of early Cambrian evolution. *Science*, 261, 1293–1298.

Bruch, A. A., Utescher, T., Mosbrugger, V., & NECLIME members (2011) Precipitation patterns in the Miocene of Central Europe and the development of continentality. *Palaeogeography, Palaeoclimatology, Palaeoecology*, 304, 202–211.
<https://doi.org/10.1016/j.palaeo.2010.10.002>

Bullen, M. E., Burbank, D. W., & Garver, J. I. (2003). Building the Northern Tien Shan: Integrated thermal, structural, and topographic constraints. *Journal of Geology*, 111, 149–165. <https://doi.org/10.1086/345840>

Caves, J. K., Bayshashov, B. U., Zhamangara, A., Ritch, A. J., Ibarra, D. E., Sjostrom, D. J., et al. (2017). Late Miocene Uplift of the Tian Shan and Altai and reorganization of Central Asia climate. *GSA Today*, 27(2), 19–26. <https://doi.org/10.1130/GSATG305A.1>

Caves, J. K., Winnick, M. J., Graham, S. A., Sjostrom, D. J., Mulch, A., & Chamberlain, P. C. (2015). Role of the westerlies in Central Asia climate over the Cenozoic. *Earth and Planetary Science Letters*, 428, 33–43. <https://doi.org/10.1016/j.epsl.2015.07.023>

Caves Rugenstein, J. K., & Chamberlain, P. C. (2018). The evolution of hydroclimate in Asia over the Cenozoic: A stable-isotope perspective. *Earth-Science Reviews*, 185, 1129–1156. <https://doi.org/10.1016/j.earscirev.2018.09.003>

Charreau, J., Chen, Y., Gilder, S., Barrier, L., Dominguez, S., Augier, R., et al. (2009). Neogene uplift of the Tian Shan Mountains observed in the magnetic record of the Jingou River section (northwest China). *Tectonics*, 28, TC2008. <https://doi.org/10.1029/2007TC002137>

Charreau, J., Chen, Y., Gilder, S., Dominguez, S., Avouac, J.-P., Sen, S., et al. (2005). Magnetostratigraphy and rock magnetism of the Neogene Kuitun He section (northwest China): Implications for Late Cenozoic uplift of the Tianshan Mountains. *Earth and Planetary Science Letters*, 230, 177–192. <https://doi.org/10.1016/j.epsl.2004.11.002>

Charreau, J., Kent-Corson, M. L., Barrier, L., Augier, R., Ritts, B. D., Chen, Y., et al. (2012). A high-resolution stable isotopic record from the Junggar Basin (NW China): implications for the paleotopographic evolution of the Tianshan Mountains. *Earth and Planetary Science Letters*, 341, 158–169. <https://doi.org/10.1016/j.epsl.2012.05.033>

de Leeuw, A., Bukowski, K., Krijgsman, W., & Kuiper, K. F. (2010). Age of the Badenian salinity crisis; impact of Miocene climate variability on the circum-Mediterranean region. *Geology*, 38, 715–718. <https://doi.org/10.1130/G30982.1>

de Leeuw, A., Tulbure, M., Kuiper, K. F., Melinte-Dobrinescu, M. C., Stoica, M., & Krijgsman, W. (2018). New $^{40}\text{Ar}/^{39}\text{Ar}$, magnetostratigraphic and biostratigraphic constraints on the termination of the Badenian Salinity Crisis: Indications for tectonic improvement of basin interconnectivity in Southern Europe. *Global and Planetary Change*, 169, 1–15. <https://doi.org/10.1016/j.gloplacha.2018.07.001>

De Vleeschouwer, D., Vhalenkamp, M., Crucifix, M., and Pälike, H. (2017). Alternating Southern and Northern Hemisphere climate response to astronomical forcing during the past 35 m.y. *Geology*, 45, 375–378. <https://doi.org/10.1130/G38663.1>

De Pelsmaecker, E., Glorie, S., Buslov, M. M., Zhimulev, F. I., Poujol, M., Korobkin, V. V., et al. (2015). Late-Paleozoic emplacement and Meso-Cenozoic reactivation of the southern Kazakhstan granitoid basement. *Tectonophysics*, 662, 416–433. <https://doi.org/10.1016/j.tecto.2015.06.014>

Dupont-Nivet, G., Krijgsman, W., Langereis, C. G., Abels, H. A., Dai, S., & Fang, X. (2007). Tibetan plateau aridification linked to global cooling at the Eocene-Oligocene transition. *Nature*, 445, 635–638. <https://doi.org/10.1038/nature05516>

Dzhamangaraeva, A. K. (1997). Pliocene charophytes from Aktau Mountain, southeastern Kazakhstan. *Geobios*, 30(4), 475–479.

Eronen, J. T., Fortelius, M., Micheels, A., Portmann, F. T., Puolamäki, K., & Janis, C. M. (2012). Neogene aridification of the Northern Hemisphere. *Geology*, 40(9), 823–826. <https://doi.org/10.1130/G33147.1>

Flower, B. P., & Kennett, J. P. (1994). The Middle Miocene climatic transition: East Antarctic ice sheet development, deep ocean circulation and global carbon cycling. *Palaeogeography, Palaeoclimatology, Palaeoecology*, 108, 537–555.

Frisch, K., Voigt, S., Voigt, T., Hellwig, A., Verestek, V., & Weber, Y. (2019). Extreme aridity prior to lake expansion deciphered from facies evolution in the Miocene Ili Basin, south-east Kazakhstan. *Sedimentology*, 66, 1716–1745.

<https://doi.org/10.1111/sed.12556>

Frisch, K., Voigt, S., Verestek, V., Appel, E., Albert, R., Gerdes, A., Arndt, I., Raddatz, J., Voigt, T., Weber, Y., & Batenburg, S. J. (2019). Stable carbon and oxygen isotopes, calcium sulphate content, and laser ablation Uranium-Lead dating of the Miocene alluvial lacustrine Aktau succession in south-east Kazakhstan. *PANGAEA*, <https://doi.pangaea.de/10.1594/PANGAEA.906094>

GeoMapApp. Available at: <http://www.geomapapp.org>

Gerdes, A., & Zeh, A. (2006). Combined U-Pb and Hf isotope LA- (MC-) ICP-MS analyses of detrital zircons: comparison with SHRIMP and new constraints for the provenance and age of an Armorican metasediment in Central Germany. *Earth and Planetary Science Letters*, 249, 47–61. <https://doi.org/10.1016/j.epsl.2006.06.039>

Gerdes, A., & Zeh, A. (2009). Zircon formation versus zircon alteration—new insights from combined U-Pb and Lu-Hf in situ LA-ICP-MS analyses, and consequences for the interpretation of Archean zircon from the Central Zone of the Limpopo Belt. *Chemical Geology*, 261, 230–243. <https://doi.org/10.1016/j.chemgeo.2008.03.005>

Godeau, N., Deschamps, P., Guihou, A., Leonide, P., Tendil, A., Gerdes, A., et al. (2018). U-Pb dating of calcite cement and diagenetic history in microporous carbonate reservoirs: Case of the Urgonian Limestone, France. *Geology*, 46, 247–250. <https://doi.org/10.1130/G39905.1>

Gupta, A. K., Yuvaraja, A., Prakasam, M., Clemens, S. C., & Velu, A. (2015). Evolution of the South Asian monsoon wind system since the late Middle Miocene. *Palaeogeography, Palaeoclimatology, Palaeoecology*, 438, 160–157. <https://doi.org/10.1016/j.palaeo.2015.08.006>

Hammer, Ø., Harper, D. A. T., & Ryan, P. D. (2001). PAST: Paleontological Statistics software package for education and data analysis. *Palaeontologica Electronica*, 4(1).

Hellwig, A., Voigt, S., Mulch, A., Frisch, K., Bartenstein, A., Pross, J., et al. (2018). Late Oligocene to Early Miocene humidity change recorded in terrestrial sequences in the Ili Basin (south-eastern Kazakhstan, Central Asia). *Sedimentology*, 65, 517–539. <https://doi.org/10.1111/sed.12390>

Hendrix, M. S., Dumitru, T. A., & Graham, S. A. (1994). Late Oligocene–Early Miocene unroofing in the Chinese Tien Shan: An early effect of the India-Asia collision. *Geology*, 22, 487–490.

Hilgen, F. J., Hinnov, L. A., Abdul Aziz, H., Abels, H. A., Batenburg, S., Bosmans, J. H.C., et al. (2015). Stratigraphic continuity and fragmentary sedimentation: The success of cyclostratigraphy as part of integrated stratigraphy. In D. G. Smith, R. J. Baley, P. M. Burgess, A. J. Fraser (Eds.), *Strata and time: Probing the gaps in our understanding*, Geological Society, London, Special Publications (Vol. 404, pp. 157–197). <https://doi.org/10.1144/SP404.12>

Hohenegger, J., Ćorić, S., & Wagreich M. (2014). Timing of the Middle Miocene Badenian stage of the Central Paratethys. *Geologica Carpathica*, 65, 55–66. <https://doi.org/10.2478/geoca-2014-0004>

Holbourn, A., Kuhnt, W., Clemens, S., Prell, W., & Andersen N. (2013). Middle to Late Miocene stepwise climate cooling: Evidence from a high-resolution deep water isotope curve spanning 8 million years. *Paleoceanography*, 28, 688–699. <https://doi.org/10.1002/2013PA002538>

Holbourn, A., Kuhnt, W., Lyle, M., Schneider, L., Romero, O., & Anderson, N. (2014). Middle Miocene climate cooling linked to intensification of eastern equatorial Pacific upwelling. *Geology*, 42, 19–22. <https://doi.org/10.1130/G34890.1>

Holbourn, A., Kuhnt, W., Schulz, M., & Erlenkeuser, H. (2005). Impacts of orbital forcing and atmospheric carbon dioxide on Miocene ice-sheet expansion. *Nature*, 438, 483–487. <https://doi.org/10.1038/nature04123>

Hui, Z., Li, J., Xu, Q., Song, C., Zhang, J., Wu, F., & Zhao, Z. (2011). Miocene vegetation and climatic changes reconstructed from a sporopollen record of the Tianshui Basin, NE Tibetan Plateau. *Palaeogeography, Palaeoclimatology, Palaeoecology*, 308, 373–382. <https://doi.org/10.1016/j.palaeo.2011.05.043>

Jahn, B.-M., Windley, B., Natal'in, B., & Dobretsov, N. (2004). Phanerozoic continental growth in Central Asia. *Journal of Asian Earth Sciences*, 23, 599–603. [https://doi.org/10.1016/S1367-9120\(03\)00124-X](https://doi.org/10.1016/S1367-9120(03)00124-X)

Karami, M. P., de Leeuw, A., Krijgsman, W., Meijer, P. Th., & Wortel, M. J. R. (2011). The role of gateways in the evolution of temperature and salinity of semi-enclosed basins: An oceanic box model for the Miocene Mediterranean Sea and Paratethys. *Global and Planetary Change*, 79, 73–88. <https://doi.org/10.1016/j.gloplacha.2011.07.011>

Kober, M., Seib, N., Kley, J., & Voigt, T. (2013). Thick-skinned thrusting in the northern Tien Shan foreland, Kazakhstan: Structural inheritance and polyphase deformation. In M. Nemčok, A. Mora, J. W. Cosgrove (Eds.), *Thick-skin-dominated orogens: From initial inversion to full accretion*, Geological Society, London, Special Publications, (Vol. 377, pp. 19–42). <https://doi.org/10.1144/SP377.7>

Kordikova, E. G. (2000). Insectivora (Mammalia) from the Lower Miocene of the Aktau Mountains, South-Eastern Kazakhstan. *Senckenbergiana Lethaea*, 80, 67–79.

Kordikova, E.G., & de Bruijn, H. (2001). Early Miocene Rodents from the Aktau Mountains (South-Eastern Kazakhstan). *Senckenbergiana Lethaea*, 81, 391–405.

Kröner, A., Kovach, V., Belousova, E., Hegner, E., Armstrong, R., Dolgoplova, A., et al. (2014). Reassessment of continental growth during the accretionary history of the

Central Asian Orogenic Belt. *Gondwana Research*, 25, 103–125.
<https://doi.org/10.1016/j.gr.2012.12.023>

Laskar, J., Robutel, P., Joutel, F., Gastineau, M., Correia, A.C.M., & Levrard, B. (2004). A long-term numerical solution for the insolation quantities of the Earth. *Astronomy & Astrophysics*, 428, 261–285. <https://doi.org/10.1051/0004-6361:20041335>

Leng, M. J., & Marshall, J. D. (2004). Paleoclimate interpretation of stable isotope data from lake sediment archives. *Quaternary Science Reviews*, 23, 811–831.
<https://doi.org/10.1016/j.quascirev.2003.06.012>

Levy, R.H., Meyers, S.R., Naish, T.R., Golledge, N.R., McKay, R.M., Crampton, J.S., et al. (2019). Antarctic ice-sheet sensitivity to obliquity forcing through ocean connections. *Nature Geoscience*, 12, 132–137. <https://doi.org/10.1038/s41561-018-0284-4>

Li, H.-C., & Ku, T.-L. (1997). $\delta^{13}\text{C}$ – $\delta^{18}\text{O}$ covariance as a paleohydrological indicator for closed-basin lakes. *Palaeogeography, Palaeoclimatology, Palaeoecology*, 133, 69–80.

Li, Q., Parrish, R. R., Horstwood, M. S. A., & McArthur, J. M. (2014). U-Pb dating of cements in Mesozoic ammonites. *Chemical Geology*, 376, 76–83.
<https://doi.org/10.1016/j.chemgeo.2014.03.020>

Licht, A., Dupont-Nivet, G., Pullen, A., Kapp, P., Abels, H. A., Lai, Z., et al. (2016). Resilience of the Asian atmospheric circulation shown by Paleogene dust provenance. *Nature Communications*, 7, 12390, <https://doi.org/10.1038/ncomms12390>

Liebrand, D., de Bakker, A. T. M., Beddow, H. M., Wilson, P. A., Bohaty, S. M., Ruessink, G. et al. (2017). Evolution of the early Antarctic ice ages. *Proceeding of the National Academy of Sciences*, 114, 3867–3872. <https://doi.org/10.1073/pnas.1615440114>

Liivamägi, S., Rodoñ, J., Bojanowski, M., Gerdes, A., Stanek, J. J., Williams, L., & Szczerba, M. (2018). Paleosols on the Ediacaran basalts of the East European Craton: a unique record of paleoweathering with minimum diagenetic overprint. *Precambrian Research*, 316, 66–82. <https://doi.org/10.1016/j.precamres.2018.07.020>

Liu, W., Liu, Z., An, Z., Sun, J., Chang, H., Wang, N., et al. (2014). Late Miocene episodic lakes in the arid Tarim Basin, western China. *Proceedings of the National Academy of Sciences*, 111, 16292–16296. <https://doi.org/10.1073/pnas.1410890111>

Liu, L., Eronen, J. T., & Fortelius, M. (2009). Significant mid-latitude aridity in the middle Miocene of East Asia. *Palaeogeography, Palaeoclimatology, Palaeoecology*, 279, 201–206.

Lucas, S. G., Aubekero, B. Z., Dzhamangaraeva, A. K., Bayshashov, B. U., & Tyutkova, L. A. (2000). Cenozoic lacustrine deposits of the Ili Basin, Southeastern Kazakhstan. In E. H. Gierlowski-Kordesch, K. R. Kelts (Eds.), *Lake basins through space and time*, AAPG Studies in Geology (Vol. 46, pp. 59–64).

Lucas, S. G., Bayshashov, B. U., Tyutkova, L. A., Zhamangara, A. K., & Aubekero, B. Z. (1997). Mammalian biochronology of the Paleogene-Neogene boundary at Aktau Mountain, eastern Kazakhstan. *Paläontologische Zeitschrift*, 71, 305–314.

Ludwig K. (2007) Isoplot 3.62. *Berkeley Geochronology Center Special Publications*, 4, 70.

Macaulay, E. A., Sobel, E. R., Mikolaichuk, A., Kohn, B., & Stuart, F. M. (2014). Cenozoic deformation and exhumation history of the Central Kyrgyz Tien Shan. *Tectonics*, 33, 135–165. <https://doi.org/10.1002/2013TC003376>

Mangenot, X., Gasparrini, M., Gerdes, A., Bonifacie, M., & Rouchon, V. (2018). An emerging thermochronometer for carbonate-bearing rocks: $\Delta_{47}/(U-Pb)$. *Geology*, 46, 1067–1070. <https://doi.org/10.1130/G45196.1>

Malinverno, A., Erba, E., & Herbert, T. D. (2010). Orbital tuning as an inverse problem: Chronology of the early Aptian oceanic anoxic event 1a (Selli Level) in the Cismon APTICORE. *Paleoceanography*, 25, PA2203. <https://doi.org/10.1029/2009PA001769>

Mandic, O., de Leeuw, A., Vuković, B., Krijgsman, W., Harzhauser, M., & Kuiper, K. (2011). Palaeoenvironmental evolution of Lake Gacko (Southern Bosnia and Herzegovina): Impact of the Middle Miocene Climatic Optimum on the Dinaride Lake

System. *Palaeogeography, Palaeoclimatology, Palaeoecology*, 299, 475–492.
<https://doi.org/10.1016/j.palaeo.2010.11.024>

Mantsis, D. F., Clement, A. C., Broccoli, A. J., & Erb, M. P. (2011). Climate feedbacks in response to changes in obliquity. *Journal of Climate*, 24, 2830–2845.
<https://doi.org/10.1175/2010JCLI3986.1>

Mantsis, D. F., Lintner, B. R., Broccoli, A. J., Erb, M. P., Clement, A. C., & Park, H.-S. (2014). The response of large-scale circulation to obliquity-induced changes in meridional heating gradients. *Journal of Climate*, 27, 5504–5516.
<https://doi.org/10.1175/JCLI-D-13-00526.1>

Meijer, N., Dupont-Nivet, G., Abels, H.A., Kaya, M.Y., Licht, A., Xiao, M., et al. (2019). Central Asian moisture modulated by proto-Paratethys Sea incursion since the Early Eocene. *Earth and Planetary Science Letters*, 510, 73–84.
<https://doi.org/10.1016/j.epsl.2018.12.031>

Methner, K., Mulch, A., Fiebig, J., Wacker, U., Gerdes, A., Graham, S. A., & Chamberlain, P. C. (2016). Rapid Middle Eocene temperature change in western North America. *Earth and Planetary Science Letters*, 450, 132–139.
<https://doi.org/10.1016/j.epsl.2016.05.053>

Meyers, S. R. (2014). Astrochron: An R Package for Astrochronology. <https://cran.r-project.org/package=astrochron>

Meyers, S. R., & Sageman, B. B. (2007). Quantification of deep-time orbital forcing by average spectral misfit. *American Journal of Science*, 307, 773–792.
<https://doi.org/10.2475/05.2007.01>

Meyers, S. R., Sageman, B. B., & Arthur, M. A. (2012). Obliquity forcing of organic matter accumulation during Oceanic Anoxic Event 2. *Paleoceanography*, 27, PA3212.
<https://doi.org/10.1029/2012PA002286>

Miao, Y., Herrmann, M., Wi, F., Yan, X., & Yang, S. (2012). What controlled Mid-Late Miocene long-term aridification in Central Asia? – Global cooling or Tibetan Plateau uplift: A review. *Earth-Science Reviews*, 112, 155–172. <https://doi.org/10.1016/j.earscirev.2012.02.003>

Miller, K. G., Mountain, G. S., the Leg 150 Shipboard Party, & Members of the New Jersey Coastal Plain Drilling Project (1996). Drilling and dating New Jersey Oligocene-Miocene sequences: Ice volume, global sea level, and Exxon records. *Science*, 271, 1092–1095.

Miller, K. G., Wright, J. D., & Fairbanks, R. G. (1991). Unlocking the ice house: Oligocene-Miocene oxygen isotopes, eustasy, and margin erosion. *Journal of Geophysical Research*, 96, 6829–6848.

Morrill, C., Small, E. E., & Sloan, L. C. (2001). Modeling orbital forcing of lake level change: Lake Gosiute (Eocene), North America. *Global and Planetary Change*, 29, 57–76. [https://doi.org/10.1016/S0921-8181\(00\)00084-9](https://doi.org/10.1016/S0921-8181(00)00084-9)

Mourik, A. A., Abels, H. A., Hilgen, F. J., Di Stefano, A., & Zachariasse, W. J. (2011). Improved astronomical age constraints for the middle Miocene climate transition based on high-resolution stable isotope records from the central Mediterranean Maltese Islands. *Paleoceanography*, 26, PA1210. <https://doi.org/10.1029/2010PA001981>

Nigmatova, S. A., Bayshashov, B. U., Zhamangara, A. K., Lucas, S. G., Bayadilov, K. O., & Kasymkhankyzy, A. (2018). The new data on biostratigraphy of the basic geological section of the continental Cenozoic deposits of Aktau Mountains (south-east Kazakhstan, Ili Basin). *News of the National Academy of Sciences of the Republic of Kazakhstan – Series of Geology and Technical Sciences*, 5, 150–162. <https://doi.org/10.32014/2018.2518-170X.21>

Palcu, D. V., Golovina, L. A., Vernyhorova, Y. V., Popov, S. V., & Krijgsman, W. (2017). Middle Miocene paleoenvironmental crises in Central Eurasia caused by changes in

marine gateway configuration. *Global and Planetary Change*, 158, 57–71.
<https://doi.org/10.1016/j.gloplacha.2017.09.013>

Pound, M. J., Haywood, A. M., Salzmann, U., & Riding, J. B. (2012). Global vegetation dynamics and latitudinal temperature gradients during the Mid to Late Miocene (15.97–5.33 Ma). *Earth-Science Reviews*, 112, 1–22.
<https://doi.org/10.1016/j.earscirev.2012.02.005>

Ramstein, G., Fluteau, F., Besse, J., & Joussaume, S. (1997). Effect of orogeny, plate motion and land sea distribution on Eurasian climate change over the past 30 million years. *Nature*, 386, 788–795.

Rosen, M. R. (1994). The importance of groundwater in playas: A review of playa classifications and the sedimentology and hydrology of playas. In M. R. Rosen (Ed.), *Paleoclimate and basin evolution of playa systems*, Geological Society of America, Special Paper (Vol. 289, pp. 1–18).

Routson, C. C., McKay, N. P., Kaufman, D. S., Erb, M. P., Goosse, H., Shuman, B. N., et al. (2019). Mid-latitude net precipitation decreased with Arctic warming during the Holocene. *Nature*, 568, 83–87. <https://doi.org/10.1038/s41586-019-1060-3>

Ryan, W. B. F., Carbotte, S. M., Coplan, J. O., O'Hara, S., Melkonian, A., Arko, R., et al. (2009). Global Multi-Resolution Topography synthesis. *Geochemistry Geophysics Geosystems*, 10, Q03014. <https://doi.org/10.1029/2008GC002332>

Schiemann, R., Lüthi, D., & Schär, C. (2009). Seasonality and interannual variability of the westerly jet in the Tibetan Plateau region. *Journal of Climate*, 22, 2940–2957.
<https://doi.org/10.1175/2008JCLI2625.1>

Saylor, B. Z., & Grotzinger J. P. (1996). Reconstruction of important Proterozoic–Cambrian boundary exposure through the recognition of thrust deformation in the Nama Group of southern Namibia. *Communications of the Geological Survey of Namibia*, 11, 1–12.

Schulz, M., & Mudelsee, M. (2002). REDFIT: Estimating red-noise spectra directly from unevenly spaced paleoclimatic time series. *Computers & Geosciences*, 28, 421–426. [https://doi.org/10.1016/S0098-3004\(01\)00044-9](https://doi.org/10.1016/S0098-3004(01)00044-9)

Shevenell, A. E., Kennett, J. P., & Lea, D. W. (2004). Middle Miocene southern ocean cooling and Antarctic cryosphere expansion. *Science*, 305, 1766–770. <https://doi.org/10.1126/science.1100061>

Shevenell, A. E., Kennett, J. P. and Lea, D. W. (2008). Middle Miocene ice sheet dynamics, deep-sea temperatures, and carbon cycling: A southern ocean perspective. *Geochemistry Geophysics Geosystems*, 9, Q02006. <https://doi.org/10.1029/2007GC001736>

Smith, M. E., Carroll, A. R., Scott, J. J., & Singer, B. S. (2014). Early Eocene carbon isotope excursion and landscape destabilization at eccentricity minima: Green River Formation of Wyoming. *Earth and Planetary Science Letters*, 403, 393–406. <https://doi.org/10.1016/j.epsl.2014.06.024>

Sobel, E. R., Chen, J., & Heermance, R. V. (2006). Late Oligocene-Early Miocene initiation of shortening in the Southwestern Chinese Tian Shan: implications for Neogene shortening rate variations. *Earth and Planetary Science Letters*, 247, 70–81. <https://doi.org/10.1016/j.epsl.2006.03.048>

Song, C., Hu, S., Han, W., Zhang, T., Fang, X., Gao, J., & Wu, F. (2014). Middle Miocene to earliest Pliocene sedimentological and geochemical records of climate change in the western Qaidam Basin on the NE Tibetan Plateau. *Palaeogeography, Palaeoclimatology, Palaeoecology*, 395, 67–76. <https://doi.org/10.1016/j.palaeo.2013.12.022>

Stacey, J. C. & Kramers, J. D. (1975). Approximation of terrestrial lead isotope evolution by a two-stage model. *Earth and Planetary Science Letters*, 26, 207–221. [https://doi.org/10.1016/0012-821X\(75\)90088-6](https://doi.org/10.1016/0012-821X(75)90088-6)

Sun, H., Yaning, C., Weihong, L., Feng, L., Yapeng, C., Xingming, H., & Yuhui, Y. (2010a). Variation and abrupt change of climate in the Ili River Basin, Xinjiang. *Journal of Geographical Sciences*, 20, 652–666. <https://doi.org/10.1007/s11442-010-0802-9>

Sun, J., Liu, W., Liu, Z., Deng, T., Windley, B. F., & Fu, B., (2017). Extreme aridification since the beginning of the Pliocene in the Tarim Basin western China. *Palaeogeography, Palaeoclimatology, Palaeoecology*, 485, 189–200. <https://doi.org/10.1016/j.palaeo.2017.06.012>

Sun, J., Ye, J., Wu, W., Ni, X., Bi, S., Zhang, Z., et al. (2010b). Late Oligocene–Miocene mid-latitude aridification and wind patterns in the Asian interior. *Geology*, 38, 515–518. <https://doi.org/10.1130/G30776.1>

Sun, J., Gong, Z., Tian, T., Jia, Y., & Windley, B. (2015). Late Miocene stepwise aridification in the Asian interior and the interplay between tectonics and climate. *Palaeogeography, Palaeoclimatology, Palaeoecology*, 421, 48–59. <https://doi.org/10.1016/j.palaeo.2015.01.001>

Sun, J., & Zhang, Z. (2009). Syntectonic growth strata and implications for late Cenozoic tectonic uplift in the northern Tian Shan, China. *Tectonophysics*, 463, 60–68. <https://doi.org/10.1016/j.tecto.2008.09.008>

Talbot, M. R. (1990). A review of the palaeohydrological interpretation of carbon and oxygen isotopic ratios in primary lacustrine carbonates. *Chemical Geology*, 80, 261–279. [https://doi.org/10.1016/0168-9622\(90\)90009-2](https://doi.org/10.1016/0168-9622(90)90009-2)

Tang, Z. H., Ding, Z. L., White, P. D., Dong, X. X., Ji, J. L., Jiang, H. C., et al. (2011). Late Cenozoic central Asian drying inferred from a palynological record from the northern Tian Shan. *Earth and Planetary Science Letters*, 302, 439–447. <https://doi.org/10.1016/j.epsl.2010.12.042>

Trampush, S. M., Hajek, E. A., Straub, K. M., & Chamberlin, E. P. (2017). Identifying autogenic sedimentation in fluvial-deltaic stratigraphy: Evaluating the effect of

outcrop-quality data on the compensation statistic. *Journal of Geophysical Research: Earth Surface*, 122, 91–113. <https://doi.org/10.1002/2016JF004067>

Valero, L., Garcés, M., Cabrera, L., Costa, E., & Sáez, A. (2014). 20 Myr of eccentricity paced lacustrine cycles in the Cenozoic Ebro Basin. *Earth and Planetary Science Letters*, 408, 183–193. <https://doi.org/10.1016/j.epsl.2014.10.007>

van Dam, J.A. (2006). Geographic and temporal patterns in the Late Neogene (12–3 Ma) aridification of Europe: The use of small mammals as paleoprecipitation proxies. *Palaeogeography, Palaeoclimatology, Palaeoecology*, 238, 190–218. <https://doi.org/10.1016/j.palaeo.2006.03.025>

van Dam, J. A., Abdul Aziz, H., Álvarez Sierra, M. A., Hilgen, F. J., van den Hoek Ostende, L. W., Lourens, L. J., et al. (2006). Long-period astronomical forcing on mammal turnover. *Nature*, 443, 687–691. <https://doi.org/10.1038/nature05163>

van Vugt, N., Steenbrink, J., Langereis, C. G., Hilgen, F. J., & Meulenkamp, J. E. (1998). Magnetostratigraphy-based astronomical tuning of the early Pliocene lacustrine sediments of Ptolemais (NW Greece) and bed-to-bed correlation with the marine record. *Earth and Planetary Science Letters*, 164, 535–551.

Verestek, V., Appel, E., Frisch, K., & Voigt, S. (2018). Constrained magnetostratigraphic dating of a continental middle Miocene section setting the framework for paleoclimate reconstruction in the arid central Asia. *Frontiers in Earth Science*, 6:49, <https://doi.org/10.3389/feart.2018.00049>

Voigt, S., Weber, Y., Frisch, K., Bartenstein, A., Hellwig, A., Petschick, R., et al. (2017). Climatically forced moisture supply, sediment flux and pedogenesis in Miocene mudflat deposits of south-east Kazakhstan, Central Asia. *The Depositional Record*, 3, 209–232. <https://doi.org/10.1002/dep2.34>

Wang, Z., Huang, C., Licht, A., Zhang, R., & David, K. (2019). Middle to late Miocene eccentricity forcing on lake expansion in NE Tibet. *Geophysical Research Letters*, 46, 6926–6935. <https://doi.org/10.1029/2019GL082283>

Wang, Z., Shen, Y., Licht, A., & Huang, C. (2018). Cyclostratigraphy and magnetostratigraphy of the Middle Miocene Ashigong Formation, Guide Basin, China, and its implications for the paleoclimatic evolution of NE Tibet. *Paleoceanography and Paleoclimatology*, 33, 1066–1085. <https://doi.org/10.1029/2018PA003409>

Westerhold, T., Bickert, T., & Röhl, U. (2005). Middle to late Miocene oxygen isotope stratigraphy of ODP site 1085 (SE Atlantic): new constraints on Miocene climate variability and sea-level fluctuations. *Palaeogeography, Palaeoclimatology, Palaeoecology*, 217, 205–222. <https://doi.org/10.1016/j.palaeo.2004.12.001>

Zachos, J., Pagani, M., Sloan, L., Thomas, E., & Billups, K. (2001). Trends, rhythms, and aberrations in global climate 65 Ma to present. *Science*, 292, 686–693. <https://doi.org/10.1126/science.1059412>

Zhang, T., Fang, X., Song, C., Appel, E., & Wang, Y. (2014). Cenozoic tectonic deformation and uplift of the South Tian Shan: Implications from magnetostratigraphy and balanced cross-section restoration of the Kuqa depression. *Tectonophysics*, 628, 172–187. <https://doi.org/10.1016/j.tecto.2014.04.044>

Zhang, Y., Sun, D., Li, Z., Wang, F., Wang, X., Li, B., et al. (2014). Cenozoic record of aeolian sediment accumulation and aridification from Lanzhou, China, driven by Tibetan Plateau uplift and global climate. *Global and Planetary Change*, 120, 1–15. <https://doi.org/10.1016/j.gloplacha.2014.05.009>

Zheng, H., Wei, X., Tada, R., Clift, P. D., Wang, B., Jourdan, F., et al. (2015). Late Oligocene-early Miocene birth of the Taklimakan Desert. *Proceedings of the National Academy of Sciences*, 112, 7662–7667. <https://doi.org/10.1073/pnas.1424487112>

Zhuang, G., Hourigan, J. K., Koch, P. L., Ritts, B. D., & Kent-Corson, M. L. (2011). Isotopic constraints on intensified aridity in Central Asia around 12 Ma. *Earth and Planetary Science Letters*, 312, 152–163. <https://doi.org/10.1016/j.epsl.2011.10.005>

Accepted Article

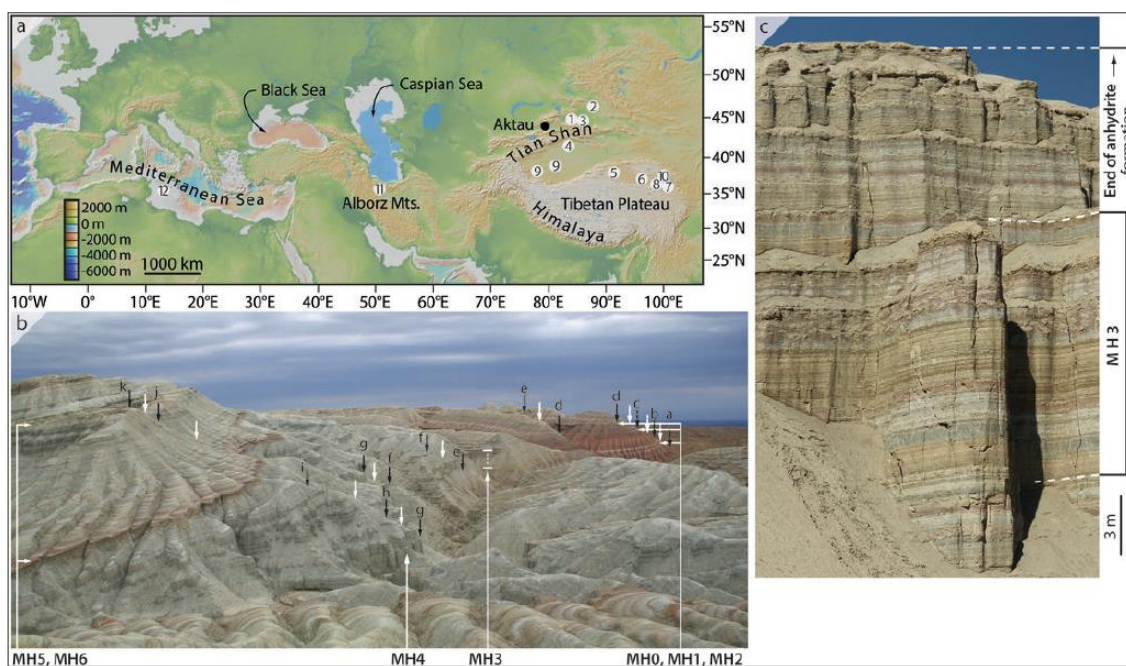


Fig. 1: Outcrop images and geographic overview of Europe and Central Asia. a: Modern topography of Europe and Central Asia with the position of the study area (Aktau, black dot) and the location of coeval paleoclimate records (numbered white dots, 1: Junggar Basin, Tang et al., 2011; 2: Junggar Basin, Sun, J. et al., 2010; 3: Junggar Basin, Charreau et al., 2012; 4: Tarim Basin, Sun et al., 2015; 5: Qaidam Basin, Song et al., 2014; 6: Qaidam Basin, Zhuang et al., 2014; 7: Tianshui Basin, Hui et al., 2011, Wang et al., 2019; 8: Guide Basin, Wang et al., 2018); 9: Tarim Basin, Zheng et al., 2015; 10: Lanzhou Basin, Zhang, Y. (2014), 11: Ballato et al. (2010); 12: Mourik et al. (2011). Modified after the GMRT digital elevation model (Ryan et al., 2009) provided by GeoMapApp. b: Panorama of the Aktau succession with indication of the marker horizons (MH0 to MH6), associated with prominent facies changes. Arrows indicate the position of long eccentricity maxima (black) and minima (white) according to the orbital tuning presented in this study. Dotted arrows localize long eccentricity maxima and minima according to the magnetostratigraphic age model. Lowercase letters define their stratigraphic sequence. c: Cyclically deposited discharge playa sediments with indication of the period of highest evaporation rates (MH3) and the end of anhydrite formation.

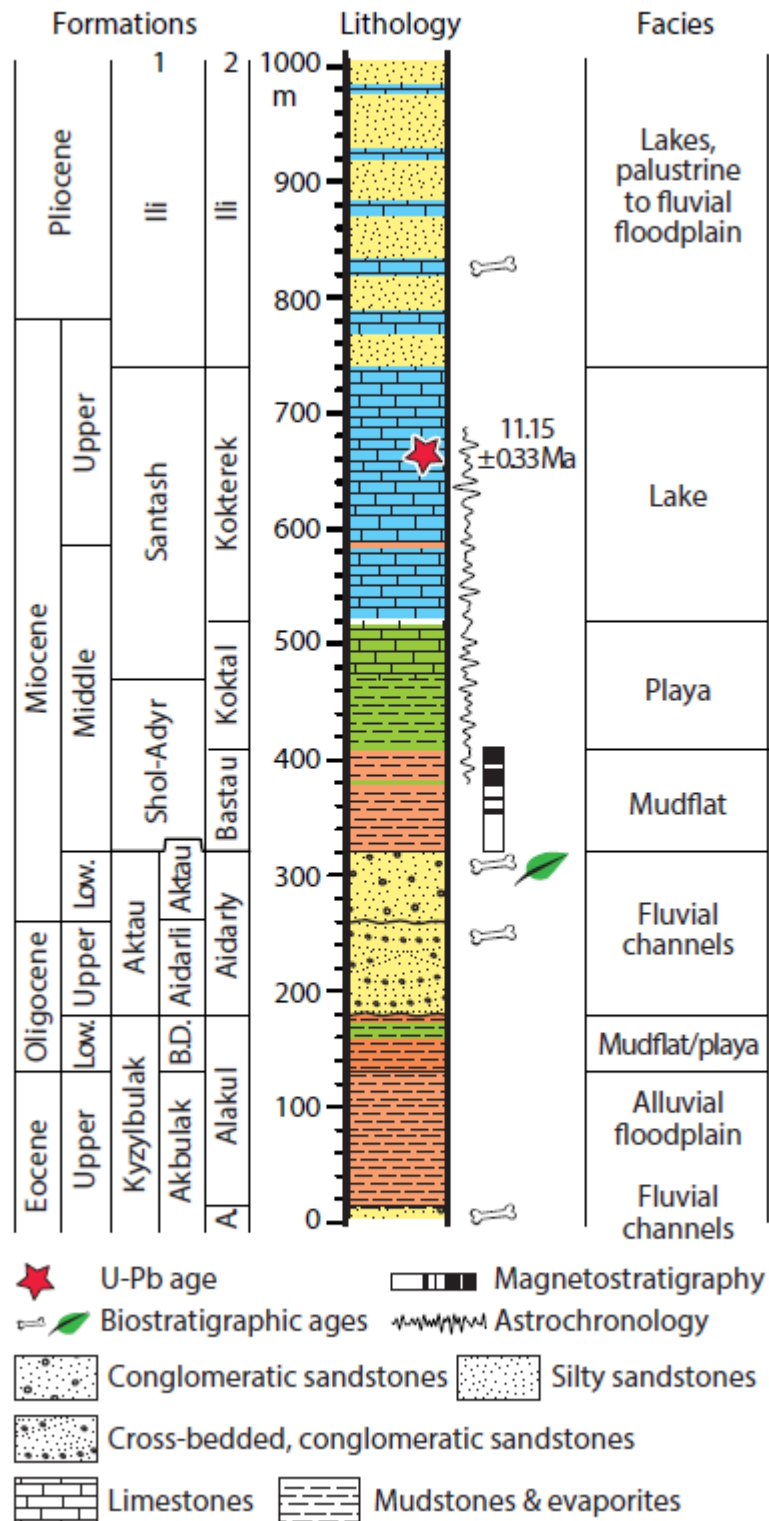


Fig. 2: Cenozoic stratigraphy of the Aktau succession. 1: after Lucas et al., (1997); Nigmatova et al. (2018), 2: This study after Bodina (1961). Abbreviations: Low.=Lower, B.D.=Betpak Dala, A.=Arasan.

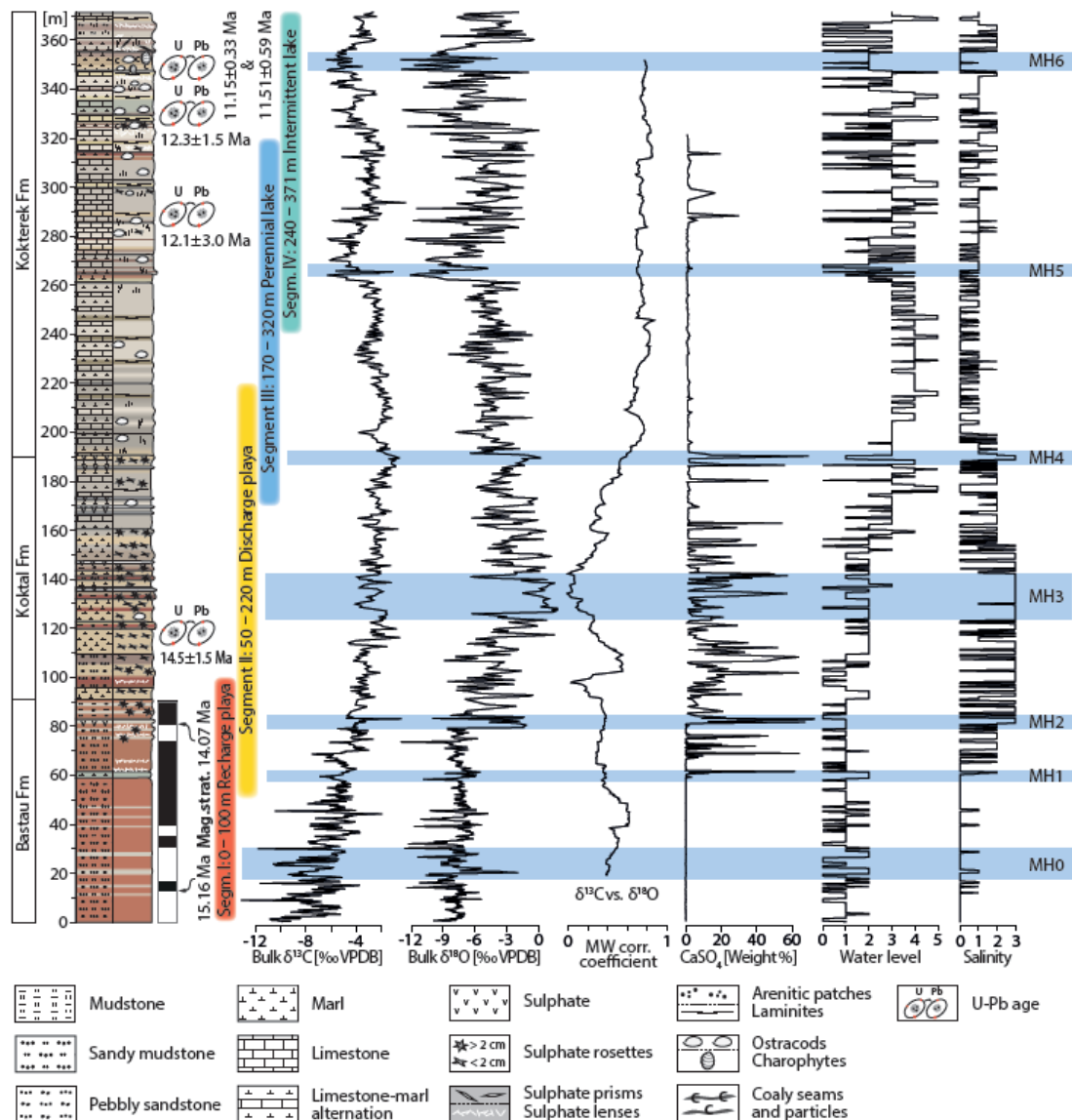


Fig. 3: Lithological log of the Aktau succession (modified after Frisch et al., 2019) with magnetostratigraphy of the Bastau Fm (Verestek et al., 2018), positions of the laser ablation U-Pb dates of carbonates, and coloured bars marking the depositional environment and segments used for time series analysis. The records of bulk-carbonate carbon and oxygen isotopes, a moving window (size: 37 m) correlation coefficient of carbonate vs. oxygen isotope values, CaSO_4 content, water level and salinity (the latter two from Frisch et al., 2019) are shown. The marker horizons MH0 to MH6 indicate prominent changes of the depositional environment. The levels 0 to 5 of the water level curve correspond to: 0=distal alluvial fan, 1=dry mudflat, 2=wet mudflat, 3=littoral lake, 4=sublittoral lake, 5=profundal lake. The salinity stages are named: 0=freshwater, 1=alkaline water, 2=saline water (gypsum precipitation), 3=saline water (anhydrite precipitation). Abbreviation: Mag.strat.=magnetostratigraphy, MW=moving window, corr.=correlation.

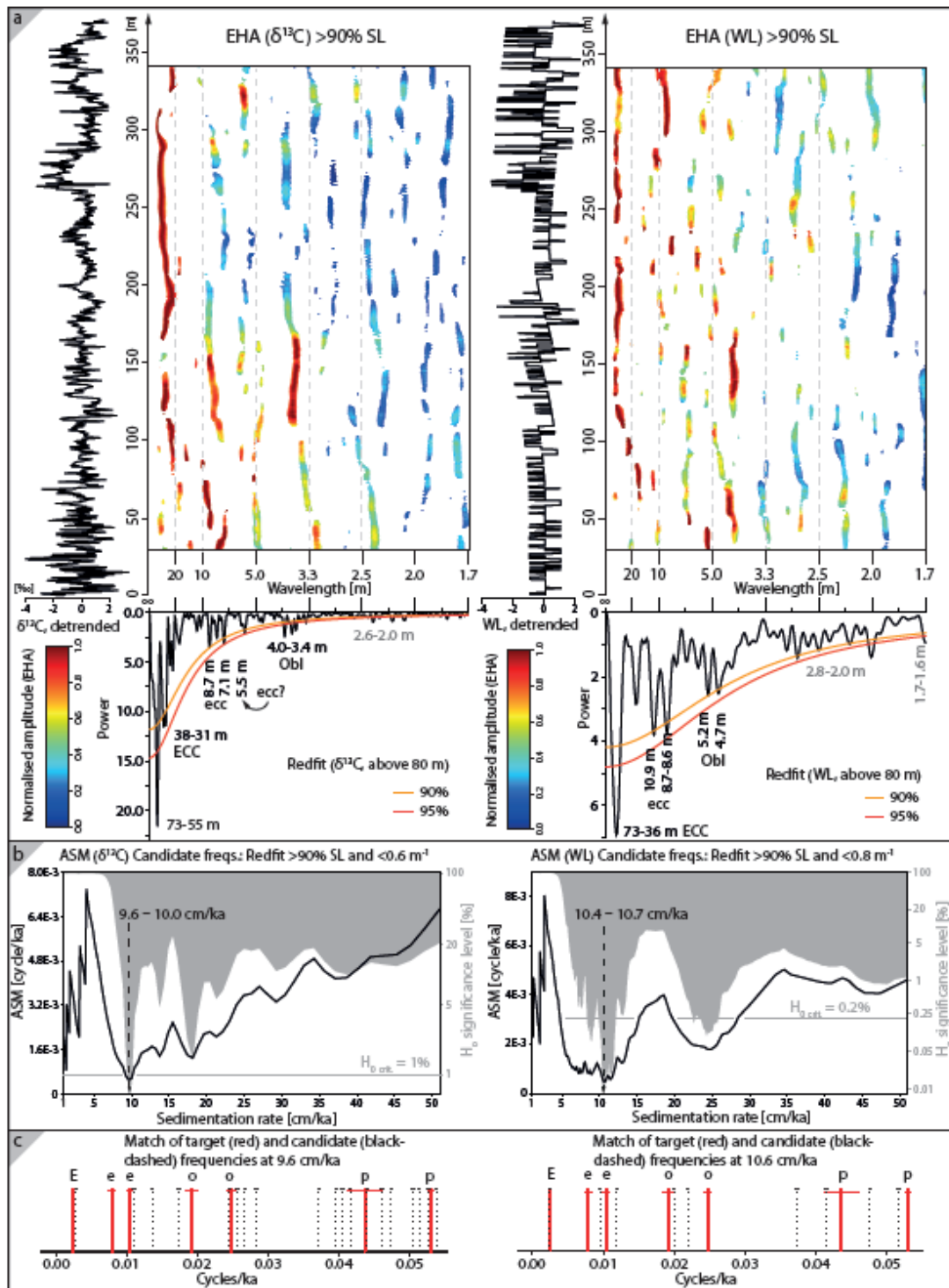


Fig. 4: Results of time series analysis of the Aktau succession based on the $\delta^{13}\text{C}$ and water level records in the depth domain. a: EHA amplitude spectra for the entire succession show a shift of the significant (>90% SL) high amplitude long wavelengths from around 20 m below 100 m to 30 to 40 m above 100 m, where this wavelength can be traced as an almost continuous band. Significant peaks of the redfit spectra (above 80 m) are tentatively labelled with their related Milankovitch cycle based on the ASM results and cycle frequency ratios. b:

ASM analysis of the $\delta^{13}\text{C}$ record (left) are calculated with the centre frequency of all significant (>90%) redfit peaks lower than 0.6 m^{-1} (candidate frequencies) using 100 distinct sedimentation rates between 1 and 51 cm ka^{-1} . The ASM null hypothesis of no orbital forcing of the candidate spectrum and frequencies can be rejected below a critical significance level $H_{0 \text{ crit.}}$ of 1%, which is true for mean sedimentation rates between 9.6 and 10.0 cm ka^{-1} . ASM analysis of the water level record (right) are calculated with the centre frequencies of all significant (>90%) redfit peaks lower than 0.8 m^{-1} (candidate frequencies) using 498 distinct sedimentation rates between 1 and 51 cm ka^{-1} . Lowest H_0 significance levels are reached at mean sedimentation rates between 10.4 and 10.7 cm ka^{-1} ($H_{0 \text{ crit.}} = 0.2\%$). c: Match of candidate frequencies (dotted black lines) and orbital target frequencies (ECC: 0.00247, ecc_1: 0.00786, ecc_2: 0.01035, obl_1: 0.01913, obl_2: 0.02475, prec_1: 0.04366, prec_2: 0.05305; values are ka^{-1} ; solid red lines) for a sedimentation rate of 9.6 cm ka^{-1} ($\delta^{13}\text{C}$) and 10.6 cm ka^{-1} (water level), respectively. Abbreviations: EHA=evolutive harmonic analysis; SL=significance level; WL=water level; ASM=average spectral misfit; freqs.=frequencies.

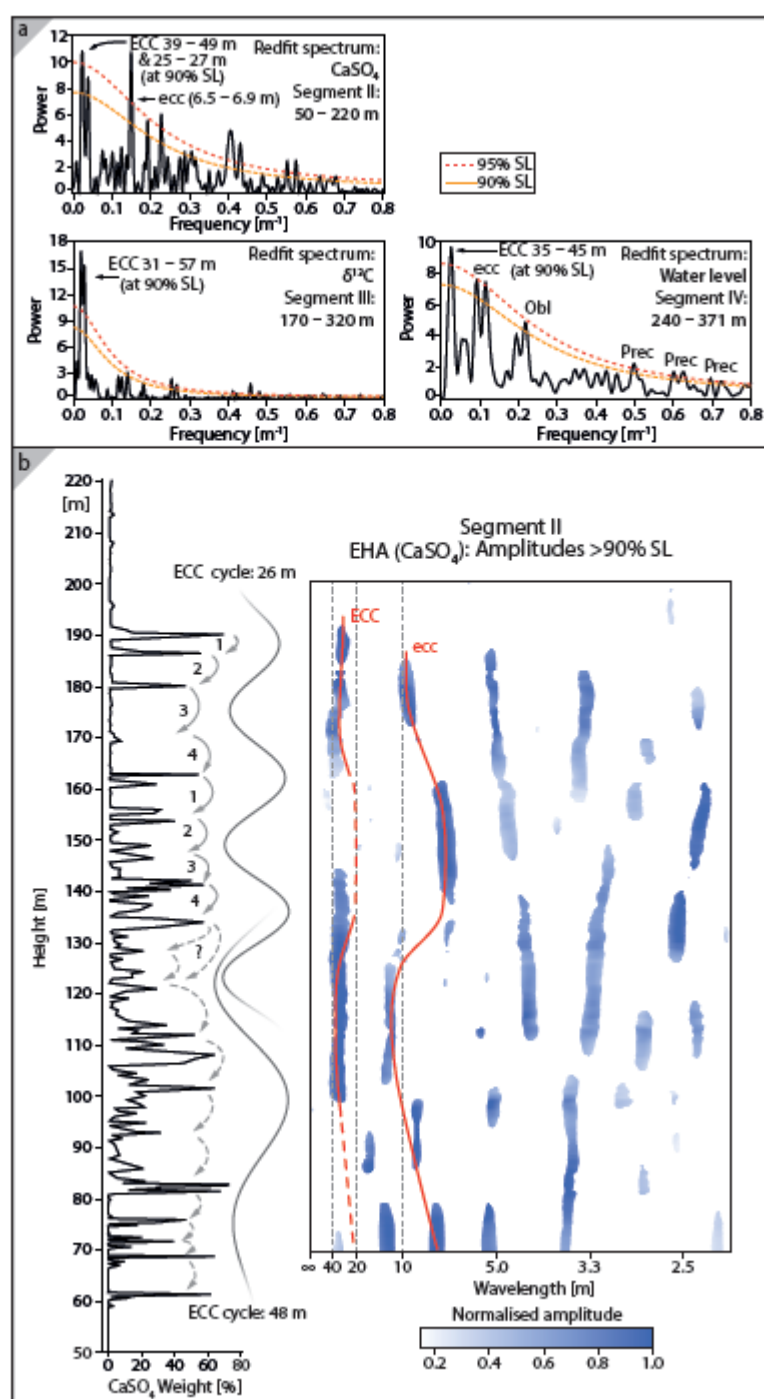


Fig. 5: Results of spectral analysis. a: Redfit spectra for the parameter $CaSO_4$, $\delta^{13}C$ and water level within the corresponding segment. Labelling of significant peaks (>90% chi square significance level) follows the interpretation of orbital cycle imprints (see text). b: Evulsive amplitude spectrum for the $CaSO_4$ record showing the course of wavelengths ascribed to long and short eccentricity forcing, with two band pass filters (48 and 26 m, filter bandwidths and center frequencies: 0.0213 centered at 0.0208 and 0.0173 centered at 0.0385, values in m^{-1}) describing the imprint of long eccentricity forcing on the $CaSO_4$ record.

Abbreviations: ECC=long eccentricity, ecc=short eccentricity, Obl=obliquity, Prec=precession, SL=significance level.

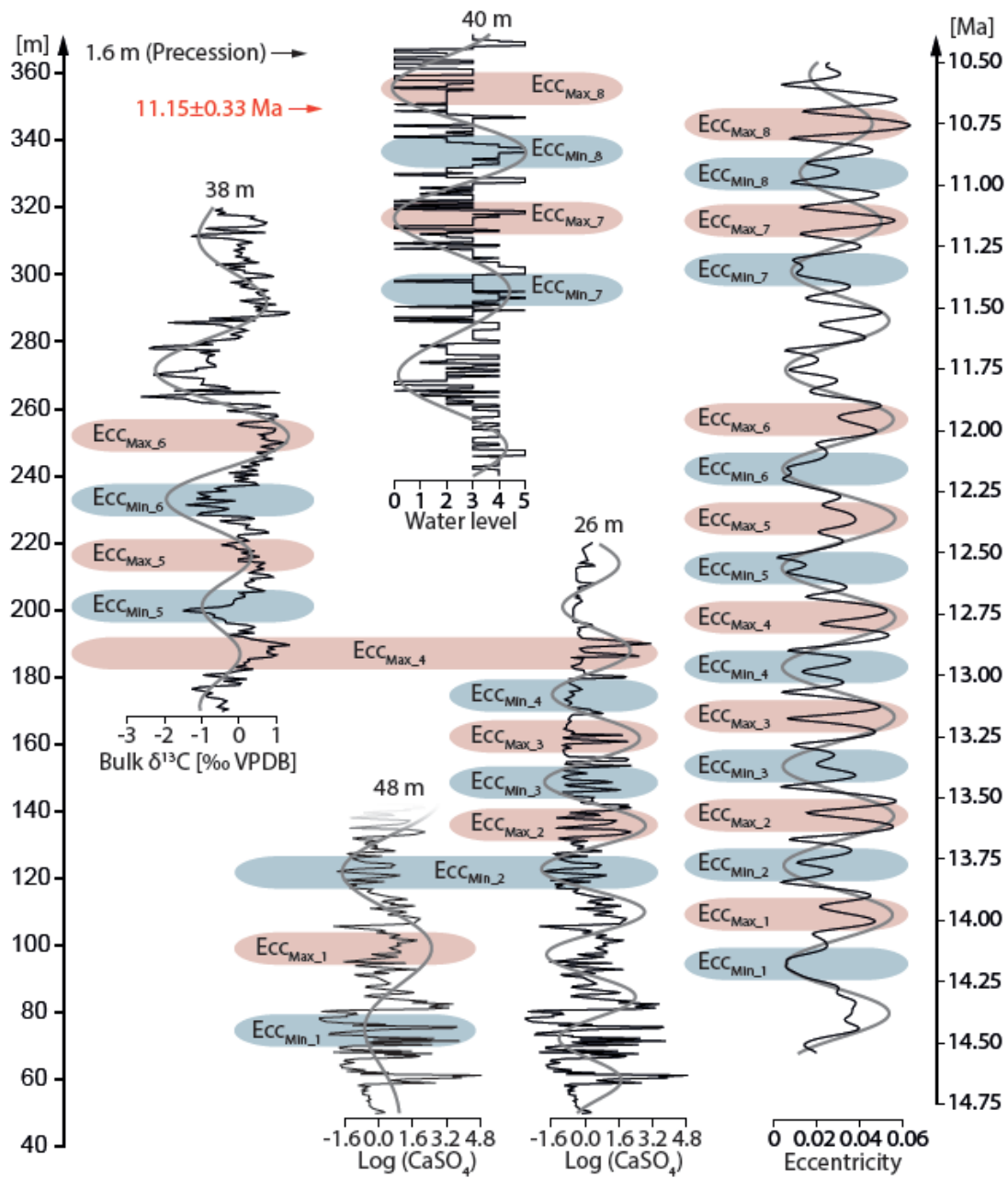


Fig. 6: Proxy records with bandpass filter outputs describing the likely long eccentricity forcing in three different segments of the Aktau succession and their tuning to the astronomical solution. See text for further explanations. Filter bandwidths and center frequencies: CaSO_4 : 0.0213 centered at 0.0208 and 0.0173 centered at 0.0385. $\delta^{13}\text{C}$: 0.0275 centered at 0.0263. Water level: 0.6061 centered at 0.6250 (precession), 0.03 centered at 0.025 (long eccentricity). Values are m^{-1} .

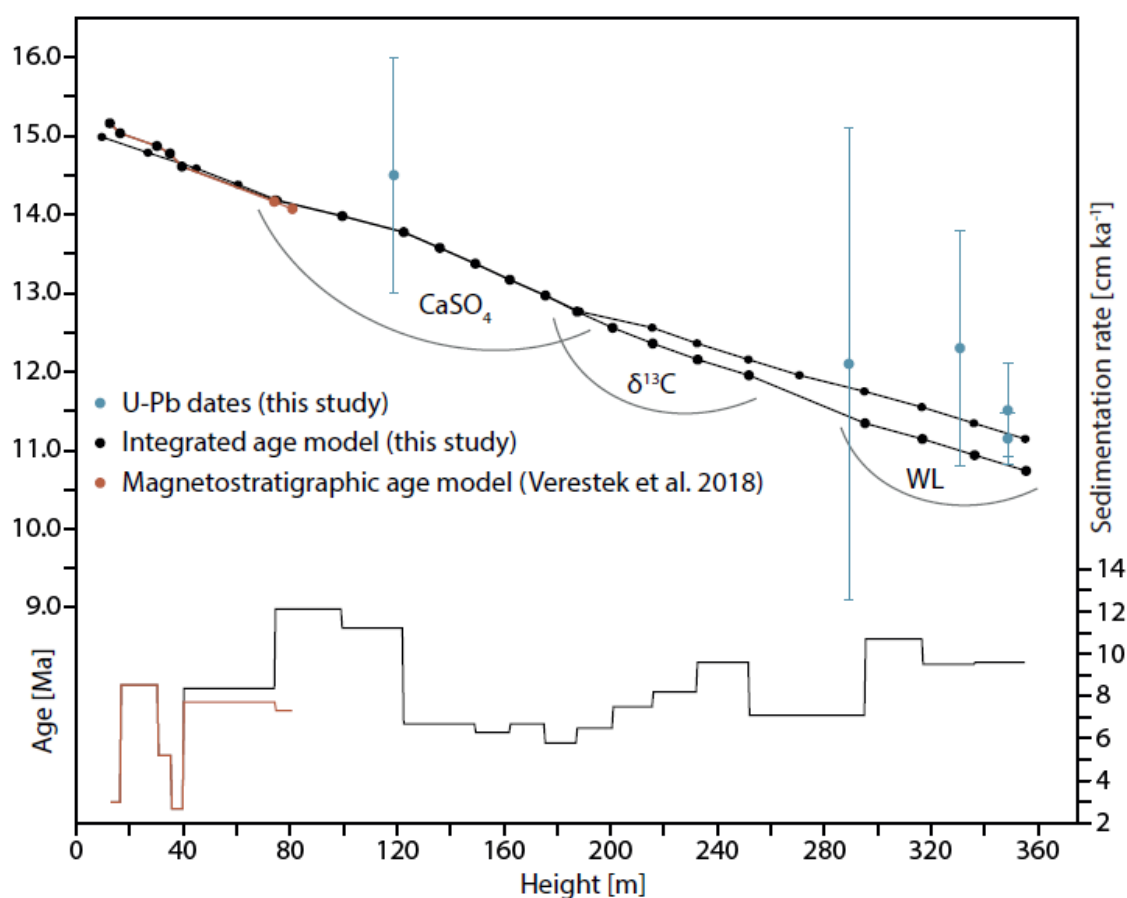


Fig. 7: Sedimentation rates and age model of the Aktau succession showing the magnetostratigraphic age model in orange (Verestek et al., 2018), the laser ablation U-Pb ages (blue) and the tie points of the integrated cyclostratigraphic and magnetostratigraphic age model (black). The segments are indicated by the brackets. In case of segment overlaps, the position of the final tie point was calculated as the mean of the two coeval tie points from each proxy record.

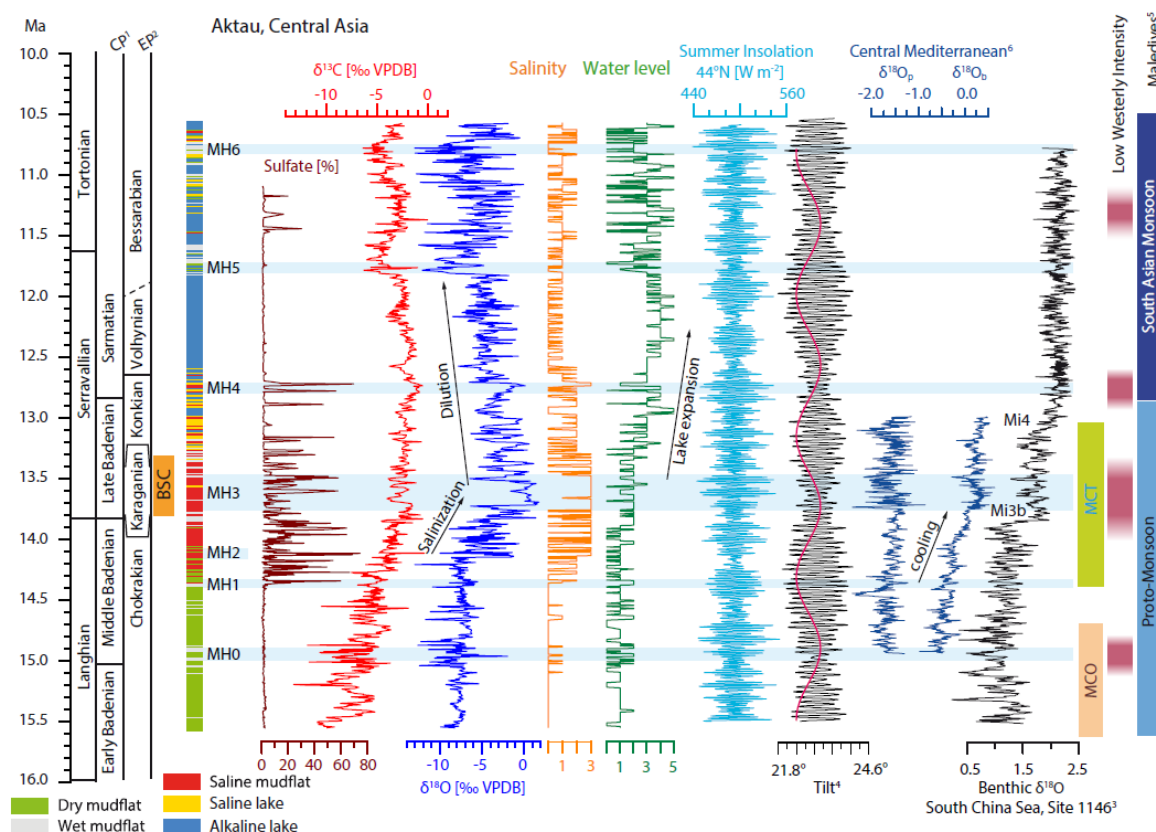


Fig. 8: Evolution of regional climate and hydrology in the Ili Basin during the Middle and early Late Miocene as inferred from CaSO_4 content, bulk-carbon and oxygen isotopes, water level, salinity and depositional environment (the latter from Frisch et al. (2019)). The red line next to the obliquity plot denotes the filtered 1.2 Ma cyclicity. References: ¹: Hohenegger et al. (2014), ²: Palcu et al. (2017), ³: Holbourn et al. (2013), ⁴: Laskar et al. (2004), ⁵: Gupta et al. (2015) and Betzler et al. (2018), ⁶: Mourik et al., (2011).